

Radiation-driven outflows from and radiative support in dusty tori of active galactic nuclei

Chi-Ho Chan and Julian H. Krolik

Department of Physics and Astronomy, Johns Hopkins University, Baltimore, MD 21218, USA

October 29, 2015

ABSTRACT

Substantial evidence points to dusty, geometrically thick tori obscuring the central engines of active galactic nuclei (AGNs), but so far no mechanism satisfactorily explains why cool dust in the torus remains in a puffy geometry. Near-Eddington infrared (IR) and ultraviolet (UV) luminosities coupled with high dust opacities at these frequencies suggest that radiation pressure on dust can play a significant role in shaping the torus. To explore the possible effects of radiation pressure, we perform three-dimensional radiative hydrodynamics simulations of an initially smooth torus. Our code solves the hydrodynamics equations, the time-dependent multi-angle group IR radiative transfer (RT) equation, and the time-independent UV RT equation. We find a highly dynamic situation. IR radiation is anisotropic, leaving primarily through the central hole. The torus inner surface exhibits a break in axisymmetry under the influence of radiation and differential rotation; clumping follows. In addition, UV radiation pressure on dust launches a strong wind along the inner surface; when scaled to realistic AGN parameters, this outflow travels at $\sim 5000 (M/10^7 M_\odot)^{1/4} [L_{\text{UV}}/(0.1 L_E)]^{1/4} \text{ km s}^{-1}$ and carries $\sim 0.1 (M/10^7 M_\odot)^{3/4} [L_{\text{UV}}/(0.1 L_E)]^{3/4} M_\odot \text{ yr}^{-1}$, where M , L_{UV} , and L_E are the mass, UV luminosity, and Eddington luminosity of the central object respectively.

Key words: galaxies: active – galaxies: nuclei – quasars: general – methods: numerical – hydrodynamics – radiative transfer

1. INTRODUCTION

The discovery of reflected broad emission lines hidden in polarized light of type-2 active galactic nuclei (AGNs) (e.g., Antonucci & Miller 1985; Miller & Goodrich 1990) came as a revelation to AGN research in that it can only be reasonably explained by a geometrically and optically thick structure surrounding the central source. Further observations established the properties of the obscurer. The ratio of type-2 to type-1 objects implies a high torus covering fraction, although the exact value of the ratio, as well as its dependence on luminosity and redshift, is still under debate (e.g., Ueda et al. 2003; Lawrence & Elvis 2010; Merloni et al. 2014; Davies et al. 2015; Oh et al. 2015). There is unequivocal proof for dust (e.g., MacAlpine 1985); in particular, the broad ~ 1 to $\sim 100 \mu\text{m}$ bump in the spectral energy distribution (SED) is attributed to thermal radiation from warm dust (e.g., Rieke & Lebofsky 1981; Barvainis 1987; Sanders et al. 1989; Pier & Krolik 1993), and the cutoff at $\lesssim 2 \mu\text{m}$ is indicative of dust close to sublimation (e.g., Rees et al. 1969). Finally, the existence of ionization (e.g., Pogge 1989; Wilson 1996) and scattering (e.g., Pogge & De Robertis 1993; Zakamska et al. 2005, 2006) cones also signifies a small, geometrically and optically thick, toroidal structure with an opening spanning a fraction of the solid angle around the central source. Infrared (IR) interferometry has provided the first direct observation of the obscuring torus in the form of warm dust within several parsecs from the center in NGC 1068 (Wittkowski et al. 2004; Jaffe et al. 2004; Poncelet et al. 2006; Raban et al. 2009), NGC 4151 (Swain et al. 2003; Bartscher et al. 2009; Pott et al. 2010), Centaurus A (Meisenheimer et al. 2007), Circinus (Tristram et al. 2007, 2012; Tristram et al. 2014), and other nearby AGNs (Beckert et al. 2008; Hönig et al. 2012). A sample of 29 AGNs have thus far been studied in this way (Tristram et al. 2009; Kishimoto et al.

2009, 2011a,b, 2013; Bartscher et al. 2013; López-Gonzaga et al. 2016). The preponderance of evidence in favor of the torus inspires the idea that observational variations between AGN types 1 and 2 can be attributed to orientation (e.g., Barthel 1989; Antonucci 1993; Urry & Padovani 1995).

A crucial missing piece to this AGN unification picture is an understanding of torus dynamics. The torus has an aspect ratio of unity if its velocity dispersion is comparable to its orbital velocity. If the velocity dispersion were entirely due to thermal motion, hydrogen atoms at a distance r from a super-massive black hole of mass M would have temperature $\gtrsim 1.7 \times 10^6 (M/10^7 M_\odot)(r/\text{pc})^{-1} \text{ K}$, hot enough to destroy dust by sputtering (Krolik & Begelman 1988). Many models of angle-dependent obscuration in AGNs have been put forward over the past decades in an effort to solve this problem. They fall into five general categories, but as we shall show below, none of them is entirely satisfactory.

Some proposed intrinsically warped structures. For example, Phinney (1989) and Sanders et al. (1989) advanced the notion that in lieu of a torus, obscuration could be provided by a geometrically thin warped disk. The disk must stretch from ~ 1 to $\sim 10^4 \text{ pc}$ to reproduce the observed IR spectrum, at odds with the presence of well-defined ionization cones on $\sim 100 \text{ pc}$ scales, with IR interferometric observations, and with optical variability on a timescale of years (e.g., Goodrich 1989). Worse still, the covering fraction is less than half except for the most severe warps and twists, and twists are imperative if one must obstruct more than half of the lines of sight at high inclinations. Parsec-scale warps and twists have garnered recent attention, with proponents arguing that they can be sustained by stochastic accretion of clumps from random directions (Lawrence & Elvis 2010; Hopkins et al. 2012), or that they are bending modes excited by radial flows caused by a lopsided disk (Hopkins et

al. 2012). However, the torus advocated by Lawrence & Elvis (2010) still suffers from the same shortcomings above, whereas the aspect ratio of the Hopkins et al. (2012) torus is only ~ 0.1 .

Another option to partially avoid the dynamical problem is dust clumping. Collisions between clumps can convert orbital shear to bulk velocity dispersion (Krolik & Begelman 1988). The collision rate must be almost once per orbit for the mid-plane to be completely covered. Should these supersonic encounters be inelastic, the resulting shocks would quickly turn the velocity dispersion of clumps into internal energy; a torus that cools efficiently would settle to the mid-plane, and one that does not would be geometrically thick, but so hot that dust is burnt away. Clumps threaded with magnetic fields could be sufficiently elastic, but the conditions are rather unusual, and one would ask how adequate field strength could be sustained.

Other workers turn to large-scale magnetic fields for an answer. Dusty molecular material lifted up from the surface of the accretion disk around the central mass could be entrained in a magnetocentrifugal wind; in this scenario, the torus is merely the parts of the wind which happen to be optically thick enough (Königl & Kartje 1994). The dust perhaps takes the form of optically thick clumps embedded in the wind (Elitzur & Shlosman 2006; see also Kartje et al. 1999). Alternatively, magnetic fields could directly support a static torus against gravity (Lovelace et al. 1998). Magnetic models, however, require strong, ordered fields on large scales, which are difficult to justify.

Still another alternative is to invoke the nuclear starbursts seen in some Seyfert 2s (e.g., Heckman et al. 1997; González Delgado et al. 2001; Cid Fernandes et al. 2001; Davies et al. 2007). They prompted Wada & Norman (2002) to suggest turbulence stirred up by supernovae as a means of creating a quasi-stable torus, but its size needs to be $\gtrsim 30$ pc, and even then the covering fraction is $\lesssim 0.2$. The obscuring gas disk of Hopkins et al. (2016) has similar drawbacks in that its size and aspect ratio are $\gtrsim 10$ pc and $\lesssim 0.3$. Stellar feedback is in fact too weak to keep the torus geometrically thick on parsec scales (Krolik & Begelman 1988). Attacking the problem from a different perspective, Schartmann et al. (2009) considered mass and energy injection by stars in a spherical and isotropic nuclear cluster. Filaments in that scheme are formed by shock waves from supernovae and planetary nebulae interacting with one another, while cold clumps come from cooling. An analogous proposal by Hueyotl-Zahuantitla et al. (2013) looked at supernova ejecta and stellar winds released with some angular momentum. The gas cools and is compressed to filaments, which then flows inward and accumulates at the centrifugal barrier, forming a torus made geometrically thick by X-ray heating. Both models attempt to circumvent the weakness of stellar feedback by injecting gas at the positions of the stars of a spatially extended cluster, hence the fate of the torus is unclear once the starburst ends. Moreover, the specific mass injection rate in the latter model is $\sim 6 \times 10^3$ times the galactic specific star formation rate.

Last but not least, Pier & Krolik (1992a) realized that since dust opacity in the IR is $\gtrsim 10$ times Thomson opacity, even sub-Eddington AGN luminosities could dramatically affect the torus through radiation pressure. In their picture, ultraviolet (UV) radiation from the central source is converted to IR on the inner surface of a smooth cylindrical torus (Pier & Krolik 1992b); part of the IR radiation diffuses through the torus and supports it. Krolik (2007) revisited the problem and constructed an analytic

solution of a smooth axisymmetric torus under the combined influence of gravity and radiation; Shi & Krolik (2008) later extended his work by incorporating the effects of hard X-ray and stellar heating. Unfortunately, both models are overly simplistic in that they assume a hydrostatic torus and the diffusion approximation for the IR radiative flux.

Others have developed ideas along a similar vein. For example, Ohsuga & Umemura (1999, 2001) considered radiation pressure from both an AGN and a nuclear starburst ring, yet their obscuring structure is stable near the mid-plane only for specific parameters. Keating et al. (2012) studied a magnetocentrifugal wind accelerated by radiation from an accretion disk; the wind again depends on the existence of some postulated large-scale magnetic field. An alternative model from Wada (2012, 2015) focuses instead on turbulence generated when gas streams lifted up by radiation fall back to the mid-plane and intersect. Its conclusions can only be tentative because UV heating and radiative cooling in this model assume ionization by starlight while X-ray heating is based on stellar-mass black hole X-ray spectra, entirely ignoring AGN radiation. The model also does not treat dust destruction by sputtering at temperatures $\gtrsim 10^5$ K. In addition, the omission of reprocessed IR radiation in these three schemes renders their applicability to optically thick tori doubtful. Less directly related is the suggestion from Thompson et al. (2005) that a starburst disk with Eddington luminosity in the IR possesses a tenuous, dusty, and geometrically thick atmosphere.

In a series of articles, Dorodnitsyn & Kallman (Dorodnitsyn et al. 2011, 2012; Dorodnitsyn & Kallman 2012; Dorodnitsyn et al. 2016) investigated the effects of IR radiation pressure on dusty tori using simulations that couple hydrodynamics and radiation. Encouragingly, they found that gas evolves naturally to a geometrically thick obscuring wind. However, there are two limitations to this work. They neglected momentum deposition from direct UV illumination. More worrisome is their use of the flux-limited diffusion (FLD) approximation, which can yield radiative fluxes in completely wrong directions wherever the optical depth is comparable to or smaller than unity. This problem is especially troubling when the dynamical effect of radiation is important (e.g., Davis et al. 2012), as it is here. Roth et al. (2012) took the complementary direction of performing Monte Carlo radiative transfer (RT) on dusty gas and calculating the radiative acceleration. The fact that they find accelerations exceeding gravity emphasizes that hydrodynamics and RT should be treated together.

We adopt a different approach in this article. Our program is to conduct a series of numerical experiments designed to yield physical insight into each of the most prominent mechanisms affecting torus dynamics; by adding mechanisms one at a time, we hope to be able to distinguish their effects. Only toward the end of this process will it be appropriate to draw specific relations between our results and observable quantities. We begin in this article by presenting three-dimensional, time-dependent radiative hydrodynamics (RHD) simulations of a dusty torus that experiences radiative acceleration on dust due to UV radiation from the central source and diffuse IR radiation in the torus. Our simulations used the finite-volume hydrodynamics code Athena (Stone et al. 2008) augmented by its time-dependent RT module (Jiang et al. 2014) for IR radiation and a new long-characteristics RT module for UV radiation (Appendix A). The

code simultaneously solves the time-dependent hydrodynamics and RT equations; most notably, it solves the RT equations on a large number of grid rays rather than adopting *ad hoc* closure prescriptions. We leave other ingredients, such as magnetic fields, realistic atomic and molecular heating and cooling rates, and dust destruction by sputtering in high-temperature regions, to future iterations.

In interpreting these results, it must be remembered that since the character of the system demands mass loss from the inner surface, realistic tori *must* be resupplied externally. Our simulation, and indeed any other simulation beginning with a finite amount of mass, *cannot* portray steady-state tori. The common device of putting a large gas reservoir at large distances would impose a misleading radiative boundary condition. For this reason, any connection between simulated and real tori must be posed in terms of the rate of mass resupply necessary to secure stationarity.

We dedicate §2 to our equations and simulation parameters. Results are presented in §3, while discussion can be found in §4.

2. METHODS

We consider a cold, dusty, and optically thick torus orbiting a point mass M at the origin. Isotropic UV radiation of luminosity L_{UV} emerges from the origin. UV radiation impinging on the inner surface is absorbed by dust and re-emitted in the IR; radiation pressure from both the IR and the UV, in concert with rotation, supports the torus against gravity. Cylindrical coordinates (R, ϕ, z) are a natural choice for describing this system, although we do occasionally refer to the spherical radius $r \equiv (R^2 + z^2)^{1/2}$. From now on, the adjective ‘radial’ shall implicitly refer to the cylindrically radial direction. We also call the section of the inner surface near the mid-plane the ‘inner edge.’

2.1. Hydrodynamics

We begin by examining the equations governing the dynamics of the torus. The hydrodynamics equations are

$$\frac{\partial \rho}{\partial t} + \nabla \cdot (\rho \mathbf{v}) = 0, \quad (1)$$

$$\frac{\partial}{\partial t}(\rho \mathbf{v}) + \nabla \cdot (\rho \mathbf{v} \mathbf{v} + p \mathbf{I}) = -\rho \nabla \Phi + \mathbf{S}_{\text{IR}}^{\text{m}} + \mathbf{S}_{\text{UV}}^{\text{m}}, \quad (2)$$

$$\frac{\partial E}{\partial t} + \nabla \cdot [(E + p) \mathbf{v}] = -\rho \mathbf{v} \cdot \nabla \Phi + S_{\text{IR}}^{\text{e}} + S_{\text{UV}}^{\text{e}}. \quad (3)$$

Here ρ , \mathbf{v} , and p are gas density, velocity, and pressure. Gas temperature and total energy density are $T = p/(\rho R_{\text{ideal}})$ and $E = \frac{1}{2} \rho v^2 + p/(\gamma - 1)$, where R_{ideal} and γ are the specific ideal gas constant and the ratio of specific heats. The gravitational potential of the central mass is $\Phi(\mathbf{r}) = -GM/r$. The energy and momentum source terms due to radiation are $S_{\text{IR,UV}}^{\text{e}}$ and $\mathbf{S}_{\text{IR,UV}}^{\text{m}}$; we shall define the IR source terms in §2.2.1, and the UV source terms in Appendix A. Finally, the isotropic rank-two tensor is denoted by \mathbf{I} .

The presence of dust means that gas temperature is $\lesssim 10^5$ K, otherwise dust would be rapidly destroyed by sputtering. This temperature is much smaller than the virial temperature, hence the gas sound speed is also a tiny fraction of the orbital velocity, or $c_s/v_\phi \ll 1$. Because gas pressure alone falls far short of maintaining the geometrical thickness of the torus, it is dynamically

unimportant compared to whatever pressure that actually provides support against gravity, such as IR radiation pressure, so an approximate equation of state for the gas is entirely satisfactory. This approximation breaks down outside the torus body, particularly in the central hole where photoionization heating and Compton recoil can strongly heat the gas (Krolik & Begelman 1986; Krolik & Kriss 2001). In the interest of focusing attention on radiation-driven dynamics, in the simulations presented here we do not change the equation of state between the body and the central hole. We plan in future work to incorporate photoionization heating and related processes; the increased gas pressure in the central hole could potentially alter the shape of the inner surface.

We treat dust and gas as a single fluid with common velocity and temperature. The fact that dust contributes significantly to IR emission implies a dust temperature below sublimation. We expect hydrogen at such temperature to remain molecular and the vibrational modes of the molecule to be weakly excited; we therefore set $R_{\text{ideal}} = k_B/(2m_{\text{H}})$ and $\gamma = \frac{7}{5}$.

2.2. Radiative transfer

Dust has $\sim 10^2$ to $\sim 10^3$ times greater opacity to UV radiation than to IR radiation (e.g., Semenov et al. 2003); such a large contrast compels us to treat radiation at the two frequencies separately.

UV radiation comes from the innermost regions of an accretion disk at the origin, but the angular distribution of its radiative flux is poorly known. The classical picture of a limb-darkened disk only holds for a Newtonian, scattering-dominated, geometrically thin, and optically thick disk; disk turbulence, thermal instabilities, coronal scattering, as well as relativistic boosting, beaming, and ray-bending, could all skew the angular profile of emergent radiation. The axis of the disk also need not be aligned with that of the torus. Because we lack a detailed disk model, and because our desire is to understand physical principles rather than to provide observables, we simply allow our UV radiative flux to be isotropic instead of giving it a more complicated and more model-dependent angular distribution.

Several RT modules have already been developed for Athena. The time-independent module (Davis et al. 2012; Jiang et al. 2012) performs RT on a snapshot of the simulation, computes the Eddington tensor, and uses it to close the angular moments of the RT equation. In comparison, the time-dependent module (Jiang et al. 2014) tracks the propagation of radiation by solving the multi-angle group RT equation directly. Both modules are suited to handling diffusive IR radiation inside the torus, but we are restricted to the time-dependent module because it is the only one available for cylindrical coordinates.

None of these modules is appropriate for point-source radiation crossing the optically thin region between the central source and the torus because they concentrate radiation along directions defined by the angle grid. Contours of constant radiation energy density, instead of being spherically symmetric, show prominent spherically radial spikes coincident with the grid rays. We therefore reserve the time-dependent module for reprocessed IR radiation inside the torus. UV radiation emitted by the central source is handled with the method of long characteristics, as described in Appendix A.

2.2.1. Time-dependent IR RT

To first order in v/c , where c is the speed of light, the mixed-frame time-dependent RT equation for IR radiation interacting with gray material reads (Jiang et al. 2014)

$$\begin{aligned} \frac{1}{c} \frac{\partial I_{\text{IR}}}{\partial t} + \hat{\mathbf{n}} \cdot \nabla I_{\text{IR}} = & \left(-1 + \hat{\mathbf{n}} \cdot \frac{\mathbf{v}}{c}\right) \rho(\kappa_{\text{IR}} + \sigma_{\text{IR}}) I_{\text{IR}} \\ & + \left(1 + 3 \hat{\mathbf{n}} \cdot \frac{\mathbf{v}}{c}\right) \rho(\kappa_{\text{IR}} B + \sigma_{\text{IR}} J_{\text{IR}}) - 2\rho\sigma_{\text{IR}} \frac{\mathbf{v}}{c} \cdot \mathbf{H}_{\text{IR}} \\ & + \rho(\kappa_{\text{IR}} - \sigma_{\text{IR}}) \frac{\mathbf{v}}{c} \cdot (\mathbf{H}_{\text{IR}}^0 - \mathbf{H}_{\text{IR}}). \end{aligned} \quad (4)$$

The specific intensity integrated over the IR in the observer frame is $I_{\text{IR}}(\hat{\mathbf{n}})$; its lowest three angular moments are J_{IR} , \mathbf{H}_{IR} , and \mathbf{K}_{IR} , from which the IR radiation energy density and flux follow as $E_{\text{IR}} = (4\pi/c)J_{\text{IR}}$ and $\mathbf{F}_{\text{IR}} = 4\pi\mathbf{H}_{\text{IR}}$. The frequency-integrated blackbody mean intensity is $B(T) = ca_{\text{SB}}T^4/(4\pi)$, where a_{SB} is the radiation constant. The coupling between gas and radiation is mediated by κ_{IR} and σ_{IR} , the comoving absorption and scattering cross sections per mass in the IR. If we take the zeroth and first angular moments of equation (4), we get

$$\begin{aligned} \frac{1}{c} \frac{\partial J_{\text{IR}}}{\partial t} + \nabla \cdot \mathbf{H}_{\text{IR}} = \\ \rho\kappa_{\text{IR}}(B - J_{\text{IR}}) + \rho(\kappa_{\text{IR}} - \sigma_{\text{IR}}) \frac{\mathbf{v}}{c} \cdot \mathbf{H}_{\text{IR}}^0 \equiv -\frac{1}{4\pi} S_{\text{IR}}^e, \end{aligned} \quad (5)$$

$$\begin{aligned} \frac{1}{c} \frac{\partial \mathbf{H}_{\text{IR}}}{\partial t} + \nabla \cdot \mathbf{K}_{\text{IR}} = \\ \rho\kappa_{\text{IR}} \frac{\mathbf{v}}{c} (B - J_{\text{IR}}) - \rho(\kappa_{\text{IR}} + \sigma_{\text{IR}}) \mathbf{H}_{\text{IR}}^0 \equiv -\frac{c}{4\pi} \mathbf{S}_{\text{IR}}^m. \end{aligned} \quad (6)$$

The remaining piece to specify in equations (4) to (6) is \mathbf{H}_{IR}^0 , the first angular moment of the IR specific intensity in the fluid frame. It is related to the angular moments in the observer frame by a Lorentz transformation (Mihalas & Weibel-Mihalas 1984):

$$\mathbf{H}_{\text{IR}}^0 = \mathbf{H}_{\text{IR}} - \frac{\mathbf{v}}{c} J_{\text{IR}} - \frac{\mathbf{v}}{c} \cdot \mathbf{K}_{\text{IR}} + \mathcal{O}(v^2/c^2). \quad (7)$$

An unreasonably small time step is needed for the time-dependent RT module if $v \ll c$, but the fact that radiation relaxes to equilibrium much faster than the hydrodynamic timescale means we can circumvent the problem with the reduced speed of light approximation (Gnedin & Abel 2001; Skinner & Ostriker 2013). The details are in Appendix B; for now, it suffices to know that the approximation replaces the physical light speed c attached to the time derivatives in equations (4) to (6) with the reduced light speed \hat{c} subject to the requirement $v < \hat{c} \ll c$. An improvement to how the time-dependent RT module treats scattering is set forth in Appendix C.

2.2.2. IR and UV opacities

The chief sources of opacity in our system are dust absorption and electron scattering, which we model as

$$\kappa_{\text{IR}}(T) \equiv \bar{\kappa}_{\text{IR}} \times \frac{1}{2} \left[1 - \tanh \frac{\log_{10}(T/T_{\text{ds}})}{\Delta_{\text{ds}}} \right], \quad (8)$$

$$\kappa_{\text{UV}}(T) \equiv \bar{\kappa}_{\text{UV}} \times \frac{1}{2} \left[1 - \tanh \frac{\log_{10}(T/T_{\text{ds}})}{\Delta_{\text{ds}}} \right], \quad (9)$$

$$\sigma_{\text{IR}}(T) \equiv \kappa_{\text{T}} \times \frac{1}{2} \left[1 + \tanh \frac{\log_{10}(T/T_{\text{hi}})}{\Delta_{\text{hi}}} \right]. \quad (10)$$

In these fitting formulae, $T_{\text{ds}} \approx 1500$ K is the dust sublimation temperature (e.g., Rees et al. 1969; Rieke & Lebofsky 1981; Barvainis 1987), $T_{\text{hi}} \approx 4013$ K is the temperature at which hydrogen atoms in local thermodynamic equilibrium at a number density of 10^4 cm^{-3} are collisionally half-ionized, and $\kappa_{\text{T}} \approx 0.397 \text{ cm}^2 \text{ g}^{-1}$ is the Thomson scattering cross section per mass. The dust opacities are normalized to Thomson as $\bar{\kappa}_{\text{IR}}/\kappa_{\text{T}} = 20$ and $\bar{\kappa}_{\text{UV}}/\kappa_{\text{T}} = 80$, a choice we shall justify in §4.3; the parameters governing the transition between opacity regimes are $\Delta_{\text{ds}} = 0.05$ and $\Delta_{\text{hi}} \approx 0.196$.

2.3. Simulation setup

We now spell out in detail the initial and boundary conditions, as well as various tricks to keep the simulation stable.

2.3.1. Initial condition

The initial condition is based on the analytic solution of an axisymmetric hydrostatic torus by Krolik (2007). To summarize, the radiation energy density inside the torus is determined along the mid-plane by

$$\begin{aligned} E_{\text{IR}}^0(R, 0) \equiv (E_{\text{IR}}^0)_{\text{in}} + \frac{3GM\rho_{\text{in}}}{R_{\text{in}}} \times \\ \left\{ \frac{1}{1+\xi} \left[\left(\frac{R}{R_{\text{in}}} \right)^{-(1+\xi)} - 1 \right] - \frac{j_{\text{in}}^2}{\xi} \left[\left(\frac{R}{R_{\text{in}}} \right)^{-\xi} - 1 \right] \right\}, \end{aligned} \quad (11)$$

and everywhere else by the constant- E_{IR}^0 contours

$$\frac{1}{2} \left(\frac{z}{R_{\text{in}}} \right)^2 + \frac{1}{2} \left(\frac{R}{R_{\text{in}}} \right)^2 - \frac{1}{3} j_{\text{in}}^2 \left(\frac{R}{R_{\text{in}}} \right)^3 = \text{constant}. \quad (12)$$

Of the five free parameters, four pertain to quantities measured at the inner edge: radial coordinate R_{in} , gas density ρ_{in} , comoving IR radiation energy density $(E_{\text{IR}}^0)_{\text{in}}$, and ratio of gas orbital to Keplerian velocity j_{in} . The remaining free parameter is the radial power-law exponent ξ of gas density along the mid-plane. We distinguish between E_{IR} and E_{IR}^0 , the IR radiation energy density in the observer and fluid frames respectively. Although the radiative initial condition inside the torus is fully specified by E_{IR}^0 , the procedure for assigning I_{IR} to individual grid rays is somewhat elaborate, and is therefore relegated to Appendix D. Gas density inside the torus is given by

$$\rho(R, z) \equiv - \left[\frac{3GM}{R^2} \left(1 - j_{\text{in}}^2 \frac{R}{R_{\text{in}}} \right) \right]^{-1} \frac{\partial E_{\text{IR}}^0}{\partial R}; \quad (13)$$

in particular, $\rho(R, 0) = \rho_{\text{in}}(R/R_{\text{in}})^{-\xi}$. Gas temperature and pressure are established by thermal equilibrium between gas and radiation, to wit, $E_{\text{IR}}^0 = a_{\text{SB}}T^4$. Lastly, gas inside the torus has orbital velocity

$$\mathbf{v} \equiv j_{\text{in}} \left(\frac{GM}{R_{\text{in}}} \right)^{1/2} \hat{\mathbf{e}}_{\phi}; \quad (14)$$

in other words, $j/j_{\text{in}} = (R/R_{\text{in}})^{1/2}$, where $j \equiv v_{\phi}(R/GM)^{1/2}$. This velocity profile in fact applies to all hydrostatic radiation-supported tori in point-mass potentials (Appendix E). The torus has extent $1 < R/R_{\text{in}} < j_{\text{in}}^{-2}$ and $z^2/R_{\text{in}}^2 \leq \frac{1}{3}(j_{\text{in}}^{-2} - 1)^2(2j_{\text{in}}^2 + 1)$.

The free parameters are selected in a similar fashion to Krolik (2007). We pick $j_{\text{in}} = \frac{1}{2}$ such that the inner edge is not supported

by rotation alone, and that its vertical extent is comparable to its radial coordinate. Having

$$(E_{\text{IR}}^0)_{\text{in}} = \frac{GM\rho_{\text{in}}}{R_{\text{in}}} \quad (15)$$

ensures IR and gravitational accelerations are comparable, that is, $\|\nabla E_{\text{IR}}\|/\rho \sim GM/r^2$, although $(E_{\text{IR}}^0)_{\text{in}}$ could take on any value as long as $E_{\text{IR}}^0 \geq 0$ inside the torus. The only deviation from Krolik (2007) is in our choice that $\xi = 1$, which results in a less massive torus.

This initial condition is not an exact equilibrium since the central source may not be able to maintain the initial distribution of IR radiation energy density along the inner surface. It is not even intended to resemble the quasi-steady state of a realistic, axisymmetric, radiation-supported torus since its properties, such as its radial and vertical extent, can be arbitrarily altered by manipulating, say, the parameter j_{in} . The initial condition is merely an approximate analytic solution of a hydrostatic radiation-supported torus; as such, it is a convenient initial condition to employ.

The exterior of the torus is filled with isothermal and hydrostatic ambient material; we grant it nonzero orbital velocity because static ambient material is found to be numerically unstable. To determine the properties of the ambient material, we build upon the method used by Goldreich et al. (1986) for slender tori. The gravitational term of the force equation is clearly the gradient of some scalar field; if we stipulate polytropic gas and a power-law orbital velocity profile, then both pressure and centrifugal terms are gradients as well, and the force equation becomes an easily solvable algebraic equation. Unlike the solution of Goldreich et al. (1986), which is an expansion around some (R, z) , our solution is exact. The density, pressure, and velocity given by our method assuming a polytropic index of unity are

$$\rho_{\text{amb}}(R, z) \equiv \bar{\rho}_{\text{amb}} \exp\left[\frac{GM}{r(c_s^2)_{\text{amb}}} + \frac{(v_\phi^2/c_s^2)_{\text{amb}}}{2 - 2q_{\text{amb}}}\right], \quad (16)$$

$$p_{\text{amb}}(R, z) \equiv \rho_{\text{amb}}(R, z) \times (c_s^2)_{\text{amb}}, \quad (17)$$

$$\mathbf{v}_{\text{amb}}(R) \equiv \left(\frac{GM}{R_{\text{amb}}}\right)^{1/2} \left(\frac{R}{R_{\text{amb}}}\right)^{1-q_{\text{amb}}} \hat{\mathbf{e}}_\phi. \quad (18)$$

The center of the simulation domain R_{amb} sets the length scale of the ambient material, while the other parameters are $\bar{\rho}_{\text{amb}} = 2 \times 10^{-8} \rho_{\text{in}}$, $(c_s^2)_{\text{amb}} = GM/R_{\text{amb}}$, and $q_{\text{amb}} = 1.75$. The shear parameter must satisfy $1.5 < q_{\text{amb}} < 2$ in order that the ambient material have finite height and be stable. Since it is preferable that density and pressure vary monotonically across the torus boundary, we additionally require $\rho \geq \rho_{\text{amb}}$ and $p \geq p_{\text{amb}}$ everywhere in the initial condition.

2.3.2. Central mass and reduced speed of light

The astute reader will notice that we have evaded any mention of the value of the central mass M . This is because its choice is by far the most complicated consideration in our simulations.

Sharp discontinuities in numerical calculations are flanked by ringing artifacts, which resemble wiggles associated with the Gibbs phenomenon. These artifacts usually damp out over time; however, in the case of a cylindrical discontinuity in a gas partially supported against gravity, such as the inner edge, the

artifact grows rapidly at any spatial resolution. Experimentation with different values of c_s/v_ϕ shows that the artifact can be suppressed by demanding $c_s/v_\phi \gtrsim \text{O}(0.1)$. If c_s/v_ϕ is kept at the low end of the numerically permitted range, gas pressure should always be weak compared to gravity; as long as gas pressure is a minor influence, it should not matter if it is not as tiny as in realistic astrophysical circumstances.

These constraints determine M . The gas equilibrium temperature T_{in} at the inner edge is set by $\kappa_{\text{UV}} L_{\text{UV}}/(4\pi R_{\text{in}}^2) = \kappa_{\text{IR}} c a_{\text{SB}} T_{\text{in}}^4$; the stability requirement $R_{\text{ideal}} T_{\text{in}}/(GM/R_{\text{in}}) \gtrsim \text{O}(0.1)^2$ then becomes

$$M \lesssim \frac{R_{\text{ideal}}^2 (\kappa_{\text{UV}}/\kappa_{\text{IR}}) \left(\frac{L_{\text{UV}}}{L_E}\right) \left(\frac{T_{\text{in}}}{T_{\text{ds}}}\right)^{-2}}{G \kappa_{\text{T}} a_{\text{SB}} T_{\text{ds}}^2} \text{O}(0.1)^{-4} \\ \approx 7.58 \times 10^{-4} \left(\frac{L_{\text{UV}}/L_E}{0.1}\right) \left(\frac{T_{\text{in}}}{T_{\text{ds}}}\right)^{-2} \text{O}(0.1)^{-4} M_\odot, \quad (19)$$

with L_E being the Eddington luminosity. We use $M \approx 0.758 M_\odot$ in practice. We shall argue in §2.3.3 that our failure to simulate a torus around a genuine supermassive black hole is completely superficial.

We now consider how M affects our choice of \hat{c} . The dynamical timescale is $[R_{\text{in}}^3/(GM)]^{1/2}$, whereas the IR radiation diffusion timescale in the reduced speed of light approximation is $\rho_{\text{in}} \bar{\kappa}_{\text{IR}} [\frac{1}{2}(j_{\text{in}}^2 - 1)R_{\text{in}}]^2/\hat{c}$. Clean separation of dynamical evolution from IR radiation diffusion requires

$$\frac{\hat{c}}{(GM/R_{\text{in}})^{1/2}} \gg \rho_{\text{in}} \bar{\kappa}_{\text{IR}} R_{\text{in}} \times \frac{1}{4}(j_{\text{in}}^2 - 1)^2; \quad (20)$$

the right-hand side is an overestimate by a factor of a couple because density falls off away from the inner edge. We settle on $\hat{c} \sim 50 (GM/R_{\text{in}})^{1/2}$ as a trade-off between accuracy and computational time (see §2.3.3 for the actual value), although we find little qualitative difference even at $\hat{c} \approx 8.94 (GM/R_{\text{in}})^{1/2}$ as long as $v < \hat{c}$ everywhere.

2.3.3. Normalization and parameters

Physical quantities are hereafter normalized to their respective fiducial values. The fundamental fiducial quantities are the central mass M , the dust sublimation temperature T_{ds} , and the Thomson scattering cross section per mass κ_{T} ; all other fiducial quantities, listed in Table 1, are derived from them. In particular, L_E is the Eddington luminosity, and r_0 is the distance where the effective temperature of the radiative flux in vacuum from a source with Eddington luminosity equals $\sqrt{2}$ times the dust sublimation temperature. Note that a system in which rotational support is provided by diffusive radiation must have $\rho_0 v_0^2/r_0 \sim E_0/r_0$.

One virtue of our normalization is that, because the characteristic length scale is $r_0 \propto M^{1/2}$, the gravitational acceleration at $r = r_0$ does not depend on M . We can guarantee accelerations due to gas pressure and radiation are likewise independent of M by fixing c_s/v_ϕ and L_{UV}/L_E for each simulation. These invariances ensure that the character of the dynamics simulated differs from that for more astrophysically relevant values of M only in the magnitude of the timescale $t_0 \propto M^{1/4}$. The normalizations of other quantities, such as momentum density, could nevertheless vary with M .

Table 1. Derived fiducial quantities.

Fiducial quantity	Symbol	Definition
luminosity	L_E	$4\pi G M c / \kappa_T$
length	r_0	$[L_E / (4\pi c a_{\text{SB}} T_{\text{ds}}^4)]^{1/2}$
velocity	v_0	$(GM/r_0)^{1/2}$
time	t_0	$(GM/r_0^3)^{-1/2}$
gas density	ρ_0	$(\kappa_T r_0)^{-1}$
gas pressure	p_0	$\rho_0 v_0^2 = a_{\text{SB}} T_{\text{ds}}^4$
radiation energy density	E_0	$L_E / (4\pi r_0^2 c) = p_0$
radiative flux	F_0	$c E_0$

Now that we have a system of normalization in place, we can translate our choice $M \approx 0.758 M_\odot$ in §2.3.2 to dimensionless parameters that the simulation actually accepts, namely, $R_{\text{ideal}} = 0.05 p_0 / (\rho_0 T_{\text{ds}})$ and $c \approx 2.70 \times 10^4 v_0$.

It remains to pick the appropriate parameters for the simulations. To start with, we choose $0.10 \leq L_{\text{UV}}/L_E \leq 0.15$ in steps of 0.01 because these luminosities are high enough to hold back the infall of the torus, but low enough not to push it away too briskly. The simulation at each L_{UV} is run for about two orbits at the inner edge, at which point the radial component of velocity is positive throughout the torus body.

Three of the five parameters governing the initial condition have already been picked in §2.3.1; the remaining two will be given here. The inner edge R_{in} should be just outside the dust sublimation radius (e.g. Rees et al. 1969; Rieke & Lebofsky 1981; Barvainis 1987; Clavel et al. 1989; Sanders et al. 1989; Pier & Krolik 1993), that is, $R_{\text{in}}^2 \gtrsim r_{\text{ds}}^2 = \kappa_{\text{UV}} L_{\text{UV}} / (4\pi \kappa_{\text{IR}} c a_{\text{SB}} T_{\text{ds}}^4)$. Our initial condition puts $R_{\text{in}} = 0.8 r_0$, so that R_{in} goes from $1.26 r_{\text{ds}}$ to $1.03 r_{\text{ds}}$ as L_{UV}/L_E varies from 0.10 to 0.15. The reduced light speed introduced in §2.3.2 can be recast in terms of fiducial values as $\hat{c} = 50 v_0$.

The density at the inner edge is selected to be $\rho_{\text{in}} = \rho_0$. The radial Thomson optical depth of our initial condition along the mid-plane is

$$\int_{R_{\text{in}}}^{\infty} dR \rho \kappa_T = \rho_{\text{in}} R_{\text{in}} \kappa_T \times \begin{cases} [j_{\text{in}}^{-2(1-\xi)} - 1] / (1 - \xi), & \xi \neq 1, \\ 2 \ln j_{\text{in}}^{-1}, & \xi = 1, \end{cases} \quad (21)$$

while the vertical Thomson optical depth at $R = R_{\text{in}}$ is

$$\int_{-\infty}^{\infty} dz \rho \kappa_T = 2 \rho_{\text{in}} R_{\text{in}} \kappa_T \int_1^{j_{\text{in}}^{-2}} dx \frac{x^{-(2+\xi)} (1 - j_{\text{in}}^2 x)}{(x^2 - \frac{2}{3} j_{\text{in}}^2 x^3 - 1 + \frac{2}{3} j_{\text{in}}^2)^{1/2}}. \quad (22)$$

Our parameters yield Thomson optical depths of ≈ 1.11 and ≈ 1.01 respectively, consistent with the observed range of values (e.g., Risaliti et al. 1999). The corresponding IR optical depths are established by numerical integration to be ≈ 19.9 and ≈ 10.9 . The ratios of Thomson to IR optical depths are not $\kappa_T/\bar{\kappa}_{\text{IR}}$ due to the higher temperature and lower IR opacity near the inner edge.

The simulation domain spans $[0.3 r_0, 5 r_0] \times [-\frac{1}{4} \pi, \frac{1}{4} \pi] \times [-4 r_0, 4 r_0]$ in (R, ϕ, z) . The vertical direction is made as tall as possible to capture escaping material, while not so tall that the centrifugal barrier would cause numerical problems at the inner-radial boundary. The number of grid cells is $188 \times 33 \times 320$ in (R, ϕ, z) , and the number of grid rays per cell is 168.

2.3.4. Boundary conditions and numerical limits

Periodic hydrodynamic and radiative boundary conditions are adopted for the azimuthal direction, with the understanding that grid rays at one boundary must be rotated through $\pm \frac{1}{2} \pi$ before they can be copied to the ghost zones at the opposite boundary, to account for the fact that the simulation domain covers only a quarter of a circle (§2.3.3).

Outflow hydrodynamic boundary conditions are applied at both boundaries in the radial and vertical directions. The value of \mathbf{v} in the ghost zones is duplicated from the last physical cell, and components pointing into the simulation domain are zeroed. We then adjust ρ and p in the ghost zones at constant $c_s^2 \equiv p/\rho$ so that the pressure gradient exactly cancels the gravitational and centrifugal forces. The value of c_s^2 is the greater of p/ρ of the last physical cell and $(c_s^2)_{\text{amb}}$; bounding c_s^2 from below protects ρ and p from numerical underflow.

Outflow radiative boundary conditions are used for the outer-radial and both vertical boundaries. For grid rays pointing away from the simulation domain, we copy their values of specific intensity from the last physical cell to the ghost zones; for all other grid rays, we set their values of specific intensity to zero. We also implement a cutout boundary condition for the inner-radial boundary. Ghost zones are filled out in the same way as an outflow boundary; on top of that, for every radially inward grid ray intersecting this boundary, we trace its trajectory across the cylindrical cutout to where it re-enters the domain, and add the specific intensity of the exiting grid ray to the corresponding grid ray in the ghost zone at the re-entry point without allowing for any time delay. Since the angle grid does not vary with coordinates, the matching of exiting to re-entering grid rays is exact. Grid rays re-entering at azimuthal coordinates outside the simulation domain are wrapped back after a suitable rotation.

Limits on gas density and temperature are enforced for the sake of numerical stability. We require that ρ satisfy $\rho \geq \rho_{\text{amb}}$, and that T satisfy $10^{-3} T_{\text{ds}} \leq T \leq 10 (c_s^2)_{\text{amb}} / R_{\text{ideal}}$; if at any time ρ and T violate these conditions, we reset them to the nearest value within the acceptable range. The density floor guarantees a stable vacuum. A static pressure floor is unsatisfactory because pressure could hit the floor before density; any further drop in density would result in erroneous heating of the gas, making the overall time step unreasonably small. A better approach is to restrict temperature to within a generous range. Because $\kappa_{\text{IR,UV}} \approx 0$ when $T \gg T_{\text{ds}}$ (§2.2.2) and $R_{\text{ideal}} T_{\text{ds}} \ll (c_s^2)_{\text{amb}}$ if the torus is supported by radiation pressure, radiative heating cannot bring the gas to the temperature ceiling.

3. RESULTS

We now present the results of our simulations. It is important to remember that the simulations do not reach steady state; therefore, what we report below is the transient response of the Krolik (2007) hydrostatic torus to UV irradiation. We already see within the first two orbits that the torus will never be hydrostatic for any L_{UV} . This is because the degree of radiative support varies strongly with time and location (§3.1), because the inner surface is corrugated radially by radiation and sheared azimuthally by differential rotation (§3.2), and because mass is continually lost in the form of a radiation-driven wind from the inner surface (§§3.1 and 3.4). We do not claim our simulations represent

the only possible configuration of a torus; instead, we wish to draw qualitative conclusions that apply to any flavor of smooth, radiation-supported torus, and to let this information guide us toward constructing a more realistic torus.

3.1. Qualitative description of gas motion

For the purpose of orientation, we begin by examining the evolution of the torus in general terms, using Figure 1 as reference. Parts of the simulation domain with $z < 0$ are discarded from our figures on the grounds that we observe no breaking of symmetry about the mid-plane.

UV radiation creates two immediate effects on the inner surface. Gas at the inner surface is swept up in the radially outward direction, forming a density concentration along it. The inner surface recedes as a result, first supersonically, then subsonically; this excites a transient in the form of an acoustic density perturbation peeling away from the density concentration and propagating outward through the torus, discernible at times $t \gtrsim 1$. The perturbation is shaped like a chevron bending outward when viewed with the full range of z .

More notably, UV radiation shaves off gas at high latitudes and creates a wind, while the central hole opens up from a cylindrical to a flaring shape. There are two reasons why this gas is the most vulnerable to UV stripping. First, we designate the UV optical depth from the central source by τ_{UV} . Only gas at $\tau_{UV} \lesssim 1$ experiences substantial UV acceleration, and the $\tau_{UV} = 1$ surface slants radially outward with increasing $|z|$ in the initial condition since ρ diminishes monotonically with $|z|$. Second, let us mentally divide the solid angle as seen from the origin into infinitely many sectors, and let us study the dynamics of the gas column contained within each sector with the proviso that neighboring columns do not interact. This is akin to the approach used by Roth et al. (2012) to calculate accelerations in their simulations. The acceleration of a column of thickness Δr due to point-source UV radiation is $\propto (1 - e^{-\rho \kappa_{UV} \Delta r})/(\rho \Delta r)$, an expression that drops with increasing $\rho \Delta r$, while for any plausible initial condition of the torus, including ours (§2.3.1), $\rho \Delta r$ rises with inclination, defined as the angle from the polar axis. An intuitive way to think about the second argument is that UV radiative flux is spherically symmetric, and if it is capable of supporting an optically thick column against gravity at low latitudes, then it is fully equipped to expel an optically thin column at high latitudes.

One might think that only gas at high latitudes participates in the wind, while gas at low latitudes accelerated by UV radiation is simply rammed against the inner surface. This is untrue because gas pressure along the flaring inner surface is virtually constant. At any height above the mid-plane, UV acceleration has a component parallel to the inner surface; unchecked by pressure gradients, this component is free to peel off gas into a wind gliding outward along the inner surface. Also note that, according to equation (14), gas starting out from smaller R has smaller Rv_ϕ , so the wind preferentially removes gas with lower specific angular momentum.

Care must be exercised in reading Figure 1 after this initial phase. We shall see in §3.2 that the initially axisymmetric inner surface becomes radially corrugated at $t \gtrsim 4t_0$. For $L_{UV}/L_E = 0.11$, averaging this undulating structure in the azimuthal direction produces the illusion that the inner surface

at $t \gtrsim 6t_0$ resembles a thick shell while in fact the density concentration remains thin in any single poloidal slice. For $L_{UV}/L_E = 0.14$, the inner surface stays relatively axisymmetric; however, the fact that it moves radially outward almost as quickly as the transients excited along it gives it the appearance of multiple shells.

The radial motion subsequent to the initial phase depends on L_{UV} , which determines the IR radiative flux across the torus. For $L_{UV}/L_E \geq 0.13$, IR radiative flux is strong enough that gas velocity is radially outward in the torus body almost all the time, hence there is little doubt the torus will be driven outward. In contrast, for $L_{UV}/L_E \leq 0.12$, a region develops above and below the mid-plane at greater radial coordinates than the inner edge in which the sum of the radial components of IR and centrifugal accelerations falls slightly short of counteracting gravity, and thus the radial component of velocity is negative. The size of this region decreases with L_{UV} . Gas outside the region continues to be propelled outward, but gas inside slides slowly toward the mid-plane and inward; as it reaches the $\tau_{UV} = 1$ surface, it is flung away by UV radiation. This kind of inflow–outflow is essentially a balance between the infall of gas toward the inner edge and the ability of UV radiation to clear out the pileup. Because there is only a finite amount of gas in the simulated torus, the inflow–outflow in our simulations cannot last forever.

The density distribution at times $t \gtrsim 4t_0$ bears little resemblance to the initial condition. Gas continues to be removed in the wind, but the detailed shape of the body depends on whether vertical support due to IR radiation is stronger or weaker than gravity. For $L_{UV}/L_E \geq 0.14$, IR radiative flux is sufficiently strong to inflate the body in the vertical direction. But for $L_{UV}/L_E \leq 0.13$, the body falls toward the mid-plane, reaching a thickness comparable to the gas pressure scale height, and then expands back vertically. The density concentration along the inner surface is shaped like another chevron and is taller than the body thanks to UV radiation constantly accelerating the gas upward and outward. Although the IR covering fraction drops steadily with time, the vertically extended inner surface and the wind keep it at a value higher than would be due to the body alone.

The degree of IR radiative support differs from place to place at these late times. For all L_{UV} , IR vertical support in the chevron-shaped inner surface is generally insufficient to counteract gravity; as we move radially outward, we encounter a wedge-shaped, lower-density region in which marginal IR vertical support prevails, followed by another region of even lower density in which IR vertical support again falls short of gravity. As L_{UV} increases, IR vertical support becomes stronger more rapidly at the inner surface than further outward in the torus, such that the inner surface is completely supported against gravity at $L_{UV}/L_E = 0.15$ even when other parts of the torus are not.

Significant mass loss in the wind leads to a substantial drop in radial IR optical depth along the mid-plane over time: By $t = 10t_0$, the optical depth is less than half its initial value for $L_{UV}/L_E = 0.10$, and down to ~ 0.05 times its initial value for $L_{UV}/L_E = 0.15$. This diminution in optical depth can be quite uneven as a function of azimuthal coordinate for L_{UV}/L_E at the low end of the simulated range because, as we shall discuss in §3.2, those are the conditions in which the non-axisymmetric radial perturbation at the inner surface grows the most; at the high end of L_{UV}/L_E , axisymmetry is maintained much more

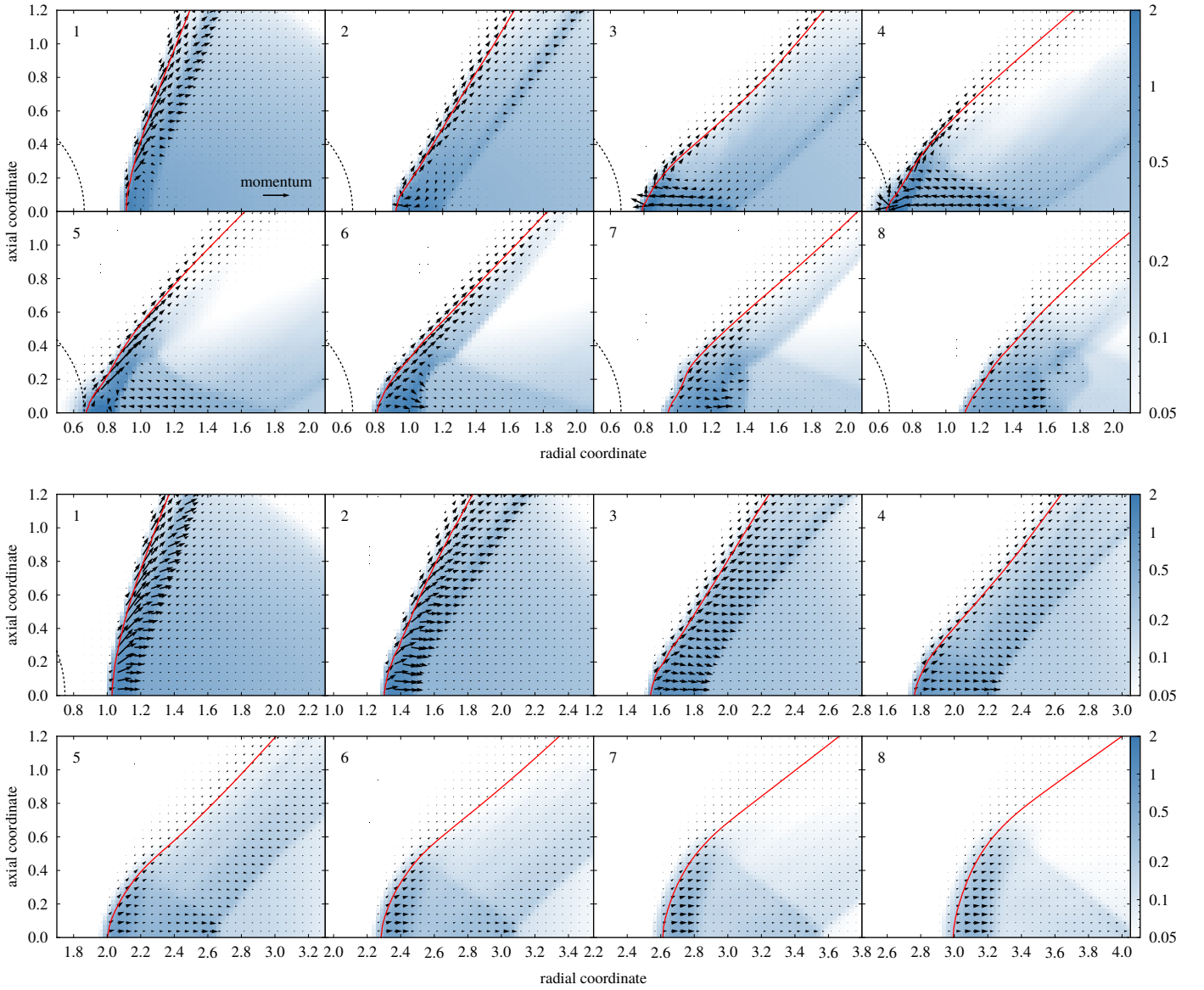


Figure 1. Zoom-in of the azimuthally averaged poloidal plane at times $t = nt_0$, where n is the number in the top-left corner of each panel. Gas density is presented on a logarithmic scale as blue intensities (see color bar along the right edge). The dust sublimation surface $r = r_{ds}$ (§2.3.3) is the dashed black curve around the origin, and the red contour traces the surface on which $\tau_{UV} = 1$. Momentum density is shown by arrows with lengths $\propto \rho v$; the arrow in the bottom-right corner of the first panel has length $0.5 \rho_0 v_0$. All quantities are normalized to fiducial units (§2.3.3). *Top grid:* Plot of the $L_{UV}/L_E = 0.11$ simulation. *Bottom grid:* Plot of the $L_{UV}/L_E = 0.14$ simulation; note that the abscissa shifts at a constant rate toward the right from panel to panel.

closely.

The rate at which UV radiation deposits momentum in the torus is proportional to the UV covering fraction, whereas the mass of the torus is roughly proportional to the covering fraction times the optical depth; hence, the sharp plunge in IR optical depth explains why the body experiences progressively stronger radially outward acceleration. For $L_{UV}/L_E \leq 0.12$, this means the inflow–outflow eventually ceases, the radial component of velocity turns positive throughout the body, and the body slides outward more and more quickly as further mass loss accompanies its outward motion.

3.2. Radial perturbation of the torus inner surface

Another intriguing complication at $t \gtrsim 4 t_0$ is the breaking of axisymmetry along the inner surface.

The three-dimensional structure of the inner surface stays remarkably vertical throughout the simulation for all L_{UV} . Isosurfaces of constant density extend almost perpendicularly upward and downward from the mid-plane until they are cut off at some height. This height depends on the density at the isosurface, and typically increases with radial coordinate due to the flaring shape of the inner surface (§3.1).

The verticality of the inner surface allows us to focus our attention on the mid-plane, as we do in Figure 2. Non-axisymmetry along the mid-plane assumes the form of a slight radial perturbation of the inner edge going through three oscillations per quarter circle at $t \sim 4 t_0$. The perturbation grows in amplitude afterward, and its behavior in the nonlinear regime depends on L_{UV} .

The top circles illustrate how, for $L_{UV}/L_E \leq 0.11$, the originally smooth inner surface breaks up into dense, thin sheets overlapping in the azimuthal direction; seen along the mid-plane, the dominant sheets resemble trailing spiral density waves. For $L_{UV}/L_E = 0.11$, the three original oscillations combine into one at $t \sim 9 t_0$; for $L_{UV}/L_E = 0.10$, the three oscillations merge into two at $t \sim 5 t_0$ and break apart into three again at $t \sim 12 t_0$.

In comparison, the bottom circles show that for $L_{UV}/L_E \geq 0.12$, the inner edge is characterized by a series of fingers pointing radially inward, connected at the outward end by arcs which are convex outward. The fingers are better described in three dimensions as vertical inward protrusions of the inner surface shaped like rounded flaps in poloidal section. The tips of the fingers and the middle portions of the arcs are slightly denser than other parts of the inner edge. The tips of the fingers are also sheared azimuthally into hooks by differential rotation. At any given time, the amplitude of the perturbation, as well as the azimuthal distortion of the fingers due to shearing, both decrease with L_{UV} .

There is nothing physical about the number three in the number of oscillations at $t \sim 4 t_0$. The initial perturbation is seeded by a small numerical artifact associated with the angle grid whose influence is the strongest at six azimuthal coordinates; the six originally tiny oscillations then merge to three easily discernible ones. Since the artifact is fixed in space while the orbital motion of the gas takes it across azimuthal coordinates, the artifact is not expected to act on the same gas packet continually; therefore, we believe the growing perturbation is a real effect.

3.3. Anisotropy of IR radiation

We now discuss the properties of IR radiation with the aid of Figure 3. Although the figure pertains to one snapshot of a single simulation, it is representative of the configuration of the torus at earlier times for all L_{UV} .

The first thing we notice in the top panel is that gas and IR radiation temperature contours coincide in the torus body, and diverge only in low-density regions outside the body. This confirms our expectation that thermal equilibrium holds deep inside the torus but not outside.

A more significant observation, verifiable by a quick inspection of the bottom panel, is that IR radiative flux streaming vertically through the central hole is stronger by a factor of a few than its nearly horizontal counterpart diffusing through the torus. This is explained by the conversion of UV radiation to IR taking place in a thin layer of thickness $\sim (\rho_{in} \kappa_{UV})^{-1}$ centered at $\tau_{UV} = 1$. The IR optical depth is $\gg 1$ from there to the outer surface, but merely $\sim \kappa_{IR}/\kappa_{UV} \ll 1$ to the central hole; consequently, it is much easier for the freshly created IR radiation to head back into the central hole than to penetrate the body.

In a geometrically and optically thick torus, some of the IR radiation emitted by the inner edge can cross the central hole, reach the far side, and be absorbed again, giving IR radiation multiple chances at breaking into the torus. However, owing to the high optical depth of the torus, the probability per attempt that IR radiation can cross the entire torus is very small, so most of the IR radiation eventually leaves in the vertical direction after a few ricochets off the inner surface. Through this process, IR radiation transfers its momentum several times to a thin layer of gas at the inner surface.

This focusing of IR radiative flux into the vertical direction means F_{IR}/F_{UV} rises gradually with r in the central hole, as seen in the bottom panel of Figure 3. A consequence is that although the wind is launched by UV radiation, IR radiation also contributes to its acceleration once it reaches altitudes comparable to the vertical extent of the torus.

We investigate \mathbf{F}_{IR} more quantitatively with Figure 4. The top panel displays $[L_{UV}/(4\pi r^2)]^{-1} \hat{\mathbf{e}}_r \cdot \mathbf{F}_{IR}$ for $L_{UV}/L_E = 0.11$ along lines emanating from the central source at various inclinations; this quantity would be unity if the IR radiative flux were spherically symmetric. The solid portions of the curves highlight the parts of the lines belonging to the torus proper. The lines are divided into two classes. Lines at high inclinations pass through the torus and have flux magnitudes below the spherically symmetric value. Conversely, lines at low inclinations lie completely within the central hole and have flux magnitudes above the spherically symmetric value; in fact, the curves appear to converge to $\sim C_{IR}/(1 - C_{IR})$ at large r , where C_{IR} is the IR covering fraction (§4.1). The increasing discrepancy from spherical symmetry toward the mid-plane illustrates the high degree of flux anisotropy.

The bottom panel of Figure 4 shows the angle between \mathbf{F}_{IR} and $\hat{\mathbf{e}}_r$. For lines at low inclinations, \mathbf{F}_{IR} is roughly parallel to $\hat{\mathbf{e}}_r$ everywhere; for lines at high inclinations, it is intriguing that the IR radiative flux snaps immediately to $\hat{\mathbf{e}}_r$ past the $\tau_{UV} = 1$ surface. The fact that \mathbf{F}_{IR} is nearly aligned with $\hat{\mathbf{e}}_r$ in the body is all the more striking considering that the IR optical depth from the inner edge to the outer surface in the vertical direction is a quarter that in the radial direction (§2.3.3).

Similar conclusions were also reached by Roth et al. (2012),

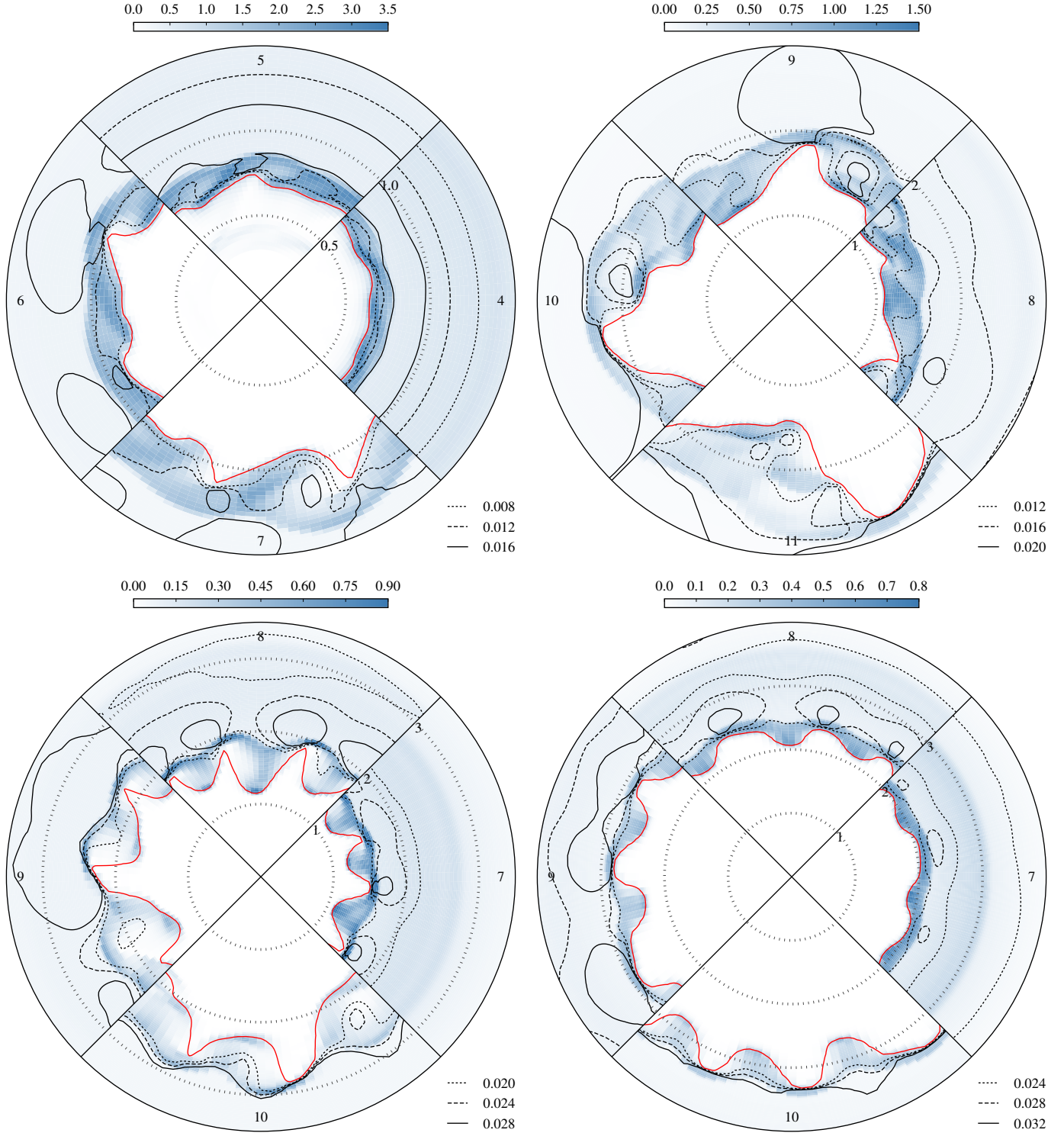


Figure 2. Mid-plane at times $t = nt_0$, where n is the number along the rim of each quadrant of the circles. Gas density is presented on a linear scale as blue intensities (see color bar above each circle), the red contour traces the surface on which $\tau_{UV} = 1$, and the black contours display $R^2 \hat{\mathbf{e}}_R \cdot \mathbf{F}_{IR}$ at levels indicated in the legend. Orbital motion is counter-clockwise, all quantities are normalized to fiducial units (§2.3.3), and all circles have different scales. *Top circles:* Plots of the $L_{UV}/L_E = 0.11$ simulation. *Bottom-left circle:* Plot of the $L_{UV}/L_E = 0.12$ simulation. *Bottom-right circle:* Plot of the $L_{UV}/L_E = 0.13$ simulation.

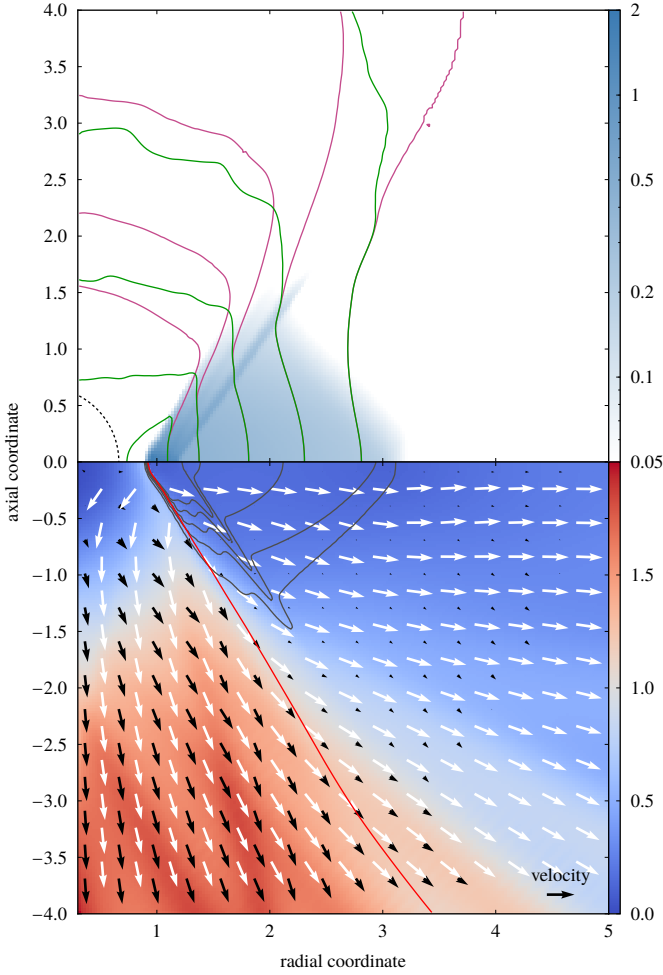


Figure 3. Azimuthally averaged poloidal plane of the $L_{UV}/L_E = 0.11$ simulation at time $t = 2t_0$, but extending farther than in the top grid of Figure 1. All quantities are normalized to fiducial units (§2.3.3). *Top panel:* Gas density is presented on a logarithmic scale as blue intensities (see color bar along the right edge). The dust sublimation surface $r = r_{ds}$ (§2.3.3) is the dashed black curve around the origin. Purple and green contours respectively show gas and IR radiation temperatures, both going from $0.3 T_{ds}$ to $0.7 T_{ds}$ in steps of $0.1 T_{ds}$ as one moves from the right to the left; to avoid confusion, contours not passing through the torus body are hidden. *Bottom panel:* The background colors display $[L_{UV}/(4\pi r^2)]^{-1} F_{IR}$ (see color bar along the right edge), which is unity for spherically symmetric radiation. The gray contours plot density rising from $0.1 \rho_0$ on the outside to $0.5 \rho_0$ on the inside in steps of $0.1 \rho_0$. The $\tau_{UV} = 1$ surface is traced by a red contour. The white and black arrows graph \mathbf{F}_{IR}/F_{IR} and \mathbf{v} respectively; the arrow in the bottom-right corner has length $5 v_0$.

who found that, for a smooth torus with geometrical thickness under a certain threshold, most of the bolometric radiative flux exits through the central hole while only a small fraction traverses the body. In addition, because $\mathbf{F}_{UV} \propto \hat{\mathbf{e}}_r$ by definition, the bolometric radiative flux is likewise spherically radial except where \mathbf{F}_{IR} deviates most from spherically radial, that is, just inside the uppermost parts of the inner surface.

Roth et al. (2012) also stated that $F_{IR} \propto r^{-2}$ at large r . The top panel of Figure 4 certainly suggests such a trend, especially for IR radiation beyond the outer surface. Nevertheless, since the radial coordinate ratio of the outer to inner edge is small, we cannot say with confidence if the inverse-square law holds inside the body. The situation is also complicated by the torus

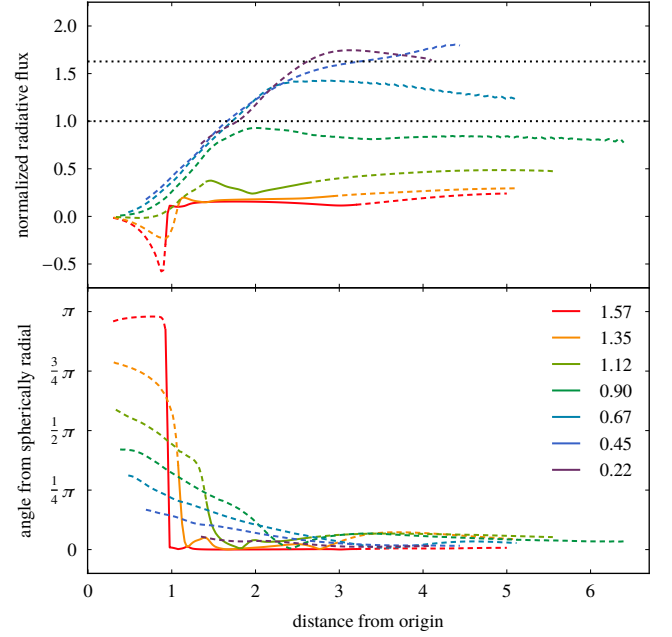


Figure 4. Azimuthally averaged IR radiative flux in the $L_{UV}/L_E = 0.11$ simulation at time $t = 2t_0$ measured along lines with inclinations indicated in the legend. The solid portion of each curve terminates at $\tau_{UV} = 1$ on the left and $\rho = (\bar{\kappa}_{IR} r_0)^{-1}$ on the right. All quantities are normalized to fiducial units (§2.3.3). *Top panel:* Plot of $[L_{UV}/(4\pi r^2)]^{-1} \hat{\mathbf{e}}_r \cdot \mathbf{F}_{IR}$; the upper and lower horizontal dotted lines are drawn at $C_{IR}/(1 - C_{IR})$ and 1. *Bottom panel:* Plot of $\arccos(\hat{\mathbf{e}}_r \cdot \mathbf{F}_{IR}/F_{IR})$.

not being in a quasi-steady state.

3.4. Mass, momentum, and kinetic energy loss rates

It is natural to ask how much mass, momentum, and kinetic energy are carried away by the UV-launched wind mentioned in §3.1. The rate at which mass is evacuated allows us to determine the ultimate fate of the torus by balancing it against possible mass resupply. Moreover, we can connect the loss rates in our simulations with observations of AGN outflows.

We emphasize that the chevron-shaped transient (§3.1) is not the wind, and that the density concentration along the inner surface (§3.1) does not trace the trajectory of individual gas packets. Since the wind encompasses a large solid angle and density range, we have no reliable way of separating it from the torus body, which is moving radially outward at the same time along the mid-plane. In practice, we define the mass loss rate as

$$\begin{aligned} \dot{M} \equiv & \int_{R=R_{\max}, |z|>r_0} R d\phi dz \hat{\mathbf{e}}_R \cdot (\rho \mathbf{v}) \\ & - \int_{z=z_{\min}} R dR d\phi \hat{\mathbf{e}}_z \cdot (\rho \mathbf{v}) \\ & + \int_{z=z_{\max}} R dR d\phi \hat{\mathbf{e}}_z \cdot (\rho \mathbf{v}), \end{aligned} \quad (23)$$

and the momentum and kinetic energy loss rates in a similar fashion; here R_{\max} and $z_{\min, \max}$ denote the coordinates of the boundaries of the simulation domain. We must be mindful to terminate our analysis before the IR half-opening angle becomes too large and the wind drops below $|z| = r_0$ at the outer-radial

boundary, at $t \gtrsim 6 t_0$. All loss rates derived from the simulations are implicitly quadrupled to account for our limited azimuthal extent (§2.3.3).

We begin with an analytic estimate of the mass loss rate. Supposing that the wind is propelled by UV momentum and reaches into $\tau_{UV} \sim 1$, the mass loss rate may be estimated by either $\dot{M} \sim L_{UV}/(c v_\infty)$ or

$$\dot{M} \sim 2 \left(\frac{2\pi R_{in}}{\rho_{in} \kappa_{UV}} \right) (\rho_{in} v_\infty) = 4\pi \frac{R_{in} v_\infty}{\kappa_{UV}}. \quad (24)$$

These two estimates agree if the wind terminal speed is

$$v_\infty \equiv \left(\frac{GM}{R_{in}} \frac{L_{UV}}{L_E} \frac{\kappa_{UV}}{\kappa_T} \right)^{1/2}. \quad (25)$$

It follows that

$$\dot{M} \sim 4\pi \left(\frac{GM R_{in}}{\kappa_T^2} \frac{L_{UV}}{L_E} \right)^{1/2} \left(\frac{\kappa_{UV}}{\kappa_T} \right)^{-1/2} \quad (26)$$

and

$$\frac{\dot{M} v_\infty^2}{L_{UV}} = \frac{v_\infty}{c} = \left(\frac{GM}{c^2 R_{in}} \frac{L_{UV}}{L_E} \frac{\kappa_{UV}}{\kappa_T} \right)^{1/2}. \quad (27)$$

When appropriately rewritten, equations (25) and (26) will also serve as the basis of our scaling relations for extrapolating our simulation results to more astrophysically relevant values of M and κ_{UV} (§4.3).

The top panel of Figure 5 demonstrates that, in keeping with this simple picture, the mass loss rates in our simulations normalized by $L_{UV}/(c v_\infty)$ are of order unity and nearly the same for all L_{UV}/L_E until $t \sim 4 t_0$.

The middle panel traces the rate at which $\hat{\mathbf{e}}_r \cdot (\rho \mathbf{v})$, the spherically radial component of gas momentum, leaves the simulation domain; the normalization is L_{UV}/c , the rate of momentum injection in the form of UV radiation. This quantity is about half for $t_0 \leq t \leq 4 t_0$, suggesting that a sizable fraction of the radiation momentum is not transferred to the gas.

We show in the bottom panel the ratio of kinetic to UV luminosity, where the kinetic luminosity is the loss rate of kinetic energy. Because $R_{in} \propto M^{1/2} (L_{UV}/L_E)^{1/2}$ (§2.3.3), equation (27) predicts $\dot{M} v_\infty^2 / L_{UV} \propto M^{1/4} (L_{UV}/L_E)^{1/4}$. The L_{UV}/L_E scaling is undetectable in our results since our range of L_{UV}/L_E spans a mere factor of 1.5; in fact, our ratio of kinetic to UV luminosity is effectively constant for all L_{UV} simulated, contrary to the $\propto L_{UV}^{1.8}$ scaling offered by Roth et al. (2012). Moreover, our explicit value is $\sim 4 \times 10^{-3}$ times that of Roth et al. (2012), but this is largely because our M is $\sim 10^{-8}$ theirs and $\dot{M} v_\infty^2 / L_{UV} \propto M^{1/4}$.

4. DISCUSSION

We now interpret our simulation results and generalize them to radiation-supported tori with different parameters.

4.1. Estimation of IR radiation energy density at the torus inner edge

The maximum of E_{IR} is attained at the inner edge because that is where UV radiation is reprocessed (§3.3). We can estimate

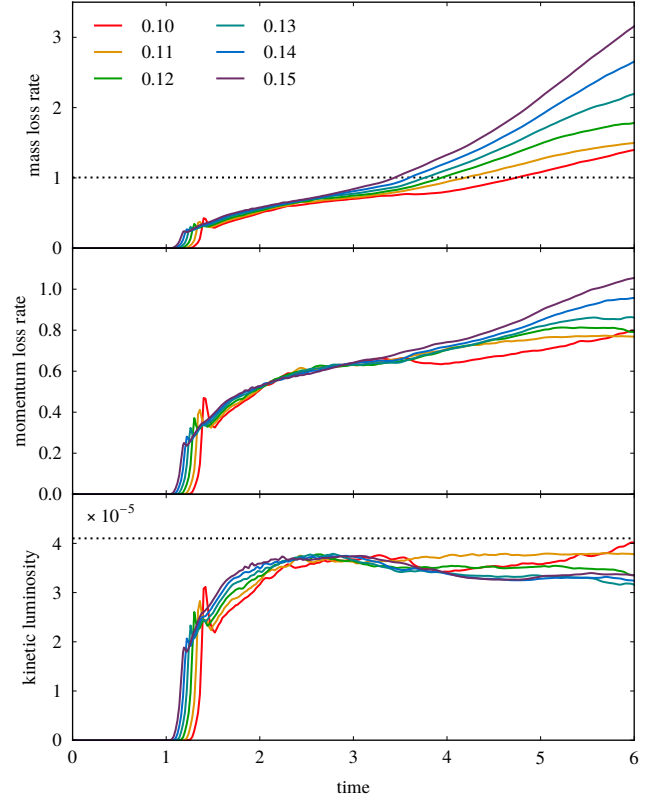


Figure 5. *Top panel:* Plot of the mass loss rate divided by $L_{UV}/(c v_\infty)$, with v_∞ from equation (25), for each value of L_{UV}/L_E indicated in the legend. The dotted line shows the mass loss rate required to deplete an isolated torus within five orbits if $L_{UV}/L_E = 0.11$. *Middle panel:* Plot of the spherically radial gas momentum loss rate divided by L_{UV}/c . *Bottom panel:* Plot of the ratio of kinetic to UV luminosity. The dotted line shows the value of $\frac{1}{3} (v_\infty/c)$ for $L_{UV}/L_E = 0.11$; the factor $\frac{1}{3}$ merely brings the line into the plot range and has no physical meaning. All quantities are normalized to fiducial units (§2.3.3).

the magnitude of the peak $(E_{IR})_{in}$ by considering the radiation energy balance at the inner edge:

$$C_{UV} \frac{L_{UV}}{4\pi R_{in}^2} + C_{IR} (F_{IR}^-)_{in} \approx (F_{IR}^+)_{in}. \quad (28)$$

We denote by $C_{IR,UV}$ the IR and UV covering fractions. Similar to the two-stream approximation, we divide the radial component of the IR radiative flux into outward and inward parts, and we assign them to F_{IR}^\pm respectively. The second term on the left-hand side represents the part of the IR radiative flux leaking from the torus through the inner edge into the central hole, and then absorbed at the far side after crossing the hole.

Equation (28) relates five variables at fixed L_{UV} and is therefore difficult to verify against our simulations; two assumptions simplify it. The first one is $C_{UV} \approx C_{IR}$. The second one comes from observing that, for IR optical depth $\Delta\tau_{IR} \gg 1$ and covering fraction $C_{IR} \lesssim 1$, IR radiation propagates diffusively at $R > R_{in}$, that is, $F_{IR}^+ + F_{IR}^- \approx c E_{IR} \gg F_{IR}^+ - F_{IR}^-$, or $F_{IR}^\pm \approx \frac{1}{2} c E_{IR}$; we suppose this holds at $R = R_{in}$ as well. Equation (28) then turns into

$$(E_{IR})_{in} \approx \frac{L_{UV}}{4\pi R_{in}^2 c} \frac{2 C_{IR}}{1 - C_{IR}}. \quad (29)$$

Our assumptions are not strictly correct because $C_{UV} > C_{IR}$,

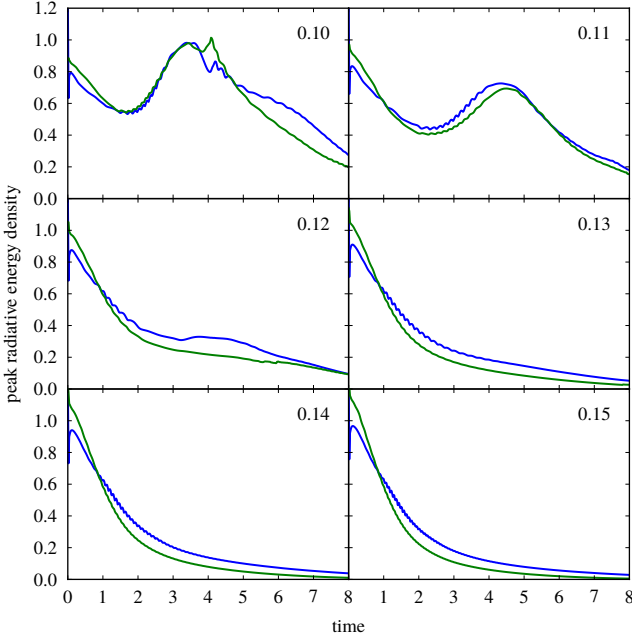


Figure 6. Plot of the left- and right-hand sides of equation (29) in blue and green curves respectively for each value of L_{UV}/L_E indicated in the top-right corner of each panel. All quantities are normalized to fiducial units (§2.3.3).

but their errors act in opposite directions in such a way that equation (29) is still an excellent description of our simulations. The factor $C_{IR}/(1 - C_{IR})$ is the number of scatterings IR radiation suffers at the inner surface prior to exit; $(E_{IR})_{in}$ goes up with C_{IR} because the torus traps IR more efficiently as C_{IR} approaches unity.

Figure 6 is a verification that, despite numerous simplifications, equation (29) captures the physics well. In preparation of this figure, we construct the radial profile of E_{IR} by azimuthally averaging its mid-plane value; we then assign $(E_{IR})_{in}$ and R_{in} to the peak of the radial profile and its radial coordinate respectively. We measure C_{IR} by considering a tight cylindrical envelope of the simulation domain, and measuring the solid angle subtended at the origin by the parts of this envelope for which the IR optical depth toward the origin is greater than unity. The success of equation (29) confirms the inner surface does act like a mirror to IR radiation.

Our study of the IR covering fraction leads to another useful result: We can predict the value of L_{UV} that marginally balances gravity in our initial condition (§2.3.1). Using equations (15) and (29), we get

$$\frac{L_{UV}}{L_E} \approx \frac{\rho_{in}}{\rho_0} \frac{R_{in}}{r_0} \frac{1 - C_{IR}}{2C_{IR}}. \quad (30)$$

The IR half-opening angle at $t = 0$ is ≈ 0.727 rad; the estimate $L_{UV}/L_E \approx 0.135$ agrees with what we have found in §3.1.

4.2. Variation of simulation parameters

It is useful to extend beyond the tiny parameter space explored by our simulations. At fixed M , the principal parameters of the system are L_{UV}/L_E , as well as ρ_{in} and j_{in} in the initial condition (§2.3.1). We ignore detailed mass and angular momentum

distributions, although interesting local effects may arise if we consider them fully. We also suppose the inner edge has temperatures near dust sublimation (e.g. Rees et al. 1969; Rieke & Lebofsky 1981; Barvainis 1987; Clavel et al. 1989; Sanders et al. 1989; Pier & Krolik 1993), so R_{in} is not a free parameter once M and L_{UV}/L_E are given. All these parameters enter into the net acceleration

$$\mathbf{a} \equiv -\frac{GM}{r^2} \hat{\mathbf{e}}_r + j^2 \frac{GM}{R^2} \hat{\mathbf{e}}_R + \frac{\kappa_{IR}}{c} \mathbf{F}_{IR} + \frac{\kappa_{UV}}{c} \mathbf{F}_{UV}, \quad (31)$$

which is a crucial factor governing torus dynamics. As far as global dynamics are concerned, it is essentially a poloidal vector with radial and vertical components $a_R \equiv \hat{\mathbf{e}}_R \cdot \mathbf{a}$ and $a_z \equiv (\text{sign } z) \hat{\mathbf{e}}_z \cdot \mathbf{a}$.

Consider how each parameter affects a_R and a_z in the torus body. Clearly a_R increases with j_{in} , while a_R and a_z increase with L_{UV}/L_E through \mathbf{F}_{IR} and \mathbf{F}_{UV} . The influence of ρ_{in} on a_R and a_z is subtler as it simultaneously controls $\Delta\tau_{IR}$ and C_{IR} , which play a role when $\Delta\tau_{IR} \gtrsim 1$. On the one hand, greater $\Delta\tau_{IR}$ reduces F_{IR} in the body according to $F_{IR} \sim c(E_{IR})_{in}/\Delta\tau_{IR}$; on the other hand, greater C_{IR} better traps IR radiation within the central hole, which at constant L_{UV}/L_E raises $(E_{IR})_{in}$ (§4.1) and thus F_{IR} in the body. Both $\Delta\tau_{IR}$ and C_{IR} rise with ρ_{in} , so it is difficult to determine which effect dominates. In short, raising j_{in} increases radial support, raising L_{UV}/L_E increases both radial and vertical support, whereas raising ρ_{in} has an indeterminate effect on support.

We now turn to local effects that can appear at the inner surface. First, consider two tori with different L_{UV}/L_E and ρ_{in} tuned so that they share \mathbf{F}_{IR} and \mathbf{a} in the body. Dynamics in the body may be identical, but \mathbf{F}_{IR} in the central hole of the torus with greater L_{UV}/L_E is necessarily stronger. Since equations (25) and (26) show that v_∞ and \dot{M} depend on L_{UV}/L_E but not ρ_{in} , this torus must host a faster wind than the other, as well as more severe losses of mass, momentum, and kinetic energy. Second, a sufficiently large increase in either L_{UV}/L_E or C_{IR} could make $(E_{IR})_{in} \gtrsim a_{SB} T_{ds}^4$ and $\kappa_{IR} \approx 0$ at the inner edge.

4.3. Scaling simulation results to more realistic parameters

As already remarked, for numerical reasons we have adopted artificially reduced values of M and κ_{UV}/κ_{IR} . Our tiny M is the result of requiring c_s/v_ϕ to be small, but not nearly as small as it would be in a real system (§2.3.2). The thickness of the UV radiation absorption layer at the inner surface is $\lesssim (\kappa_{IR}/\kappa_{UV}) \Delta\tau_{IR}^{-1}$ times the radial extent of the torus, so a large opacity ratio would entail the use of a grid size small enough to resolve an extremely thin absorption layer. Moreover, because all of the momentum in UV radiation is delivered within the layer, gas in the layer experiences an acceleration $\propto \kappa_{UV}$. With greater κ_{UV} , tracking the development of the inner surface would necessitate high temporal resolution, and the value of \hat{c} would also need to be revised upward to keep $v < \hat{c}$.

It is of course desirable to explore how the properties of our simulations might change if those two parameters were pushed to astrophysically realistic values. The true opacity ratio should be $\sim 10^2$ to $\sim 10^3$ (e.g., Semenov et al. 2003), but since the essential requirement for capturing the physics is that the correct ordering of κ_{IR} and κ_{UV} be kept, we argue our simulations are undamaged by our reduced opacity ratio. To explore the effect

of altering $\bar{\kappa}_{\text{UV}}$, we have experimented with two simulations at twice the normal spatial resolution, one with the usual value of $\bar{\kappa}_{\text{UV}}$, the other with twice the value. The inner surface recedes slightly faster and is sharper at higher $\bar{\kappa}_{\text{UV}}$, but otherwise the overall evolution of the torus and its qualitative features are unaffected.

Nevertheless, quantitative results do vary with κ_{UV} ; in particular, care must be taken when scaling the wind terminal speed and mass loss rate found in §3.4. A higher value of κ_{UV} means the optically thin wind is faster but restricted to a thinner layer. Rewriting equations (25) and (26) in terms of $R_{\text{in}}/r_{\text{ds}}$ highlights how this scaling should be performed:

$$v_{\infty} \sim (GM\kappa_{\text{T}}a_{\text{SB}}T_{\text{ds}}^4)^{1/4} \times \left(\frac{L_{\text{UV}}}{L_{\text{E}}}\right)^{1/4} \left(\frac{\kappa_{\text{IR}}\kappa_{\text{UV}}}{\kappa_{\text{T}}^2}\right)^{1/4} \left(\frac{R_{\text{in}}}{r_{\text{ds}}}\right)^{-1/2} \quad (32)$$

and

$$\dot{M} \sim 4\pi \left[\frac{(GM)^3}{\kappa_{\text{T}}^5 a_{\text{SB}} T_{\text{ds}}^4} \right]^{1/4} \times \left(\frac{L_{\text{UV}}}{L_{\text{E}}}\right)^{3/4} \left(\frac{\kappa_{\text{IR}}\kappa_{\text{UV}}}{\kappa_{\text{T}}^2}\right)^{-1/4} \left(\frac{R_{\text{in}}}{r_{\text{ds}}}\right)^{1/2}. \quad (33)$$

These forms cleanly separate the dependence on M and κ_{UV} from everything else.

Shifting the fiducial values of these parameters from those used in our simulations to more astrophysical numbers changes the wind terminal speed and mass loss rate found in our simulations to

$$v_{\infty} \sim 5000 \left(\frac{M}{10^7 M_{\odot}}\right)^{1/4} \left(\frac{L_{\text{UV}}/L_{\text{E}}}{0.1}\right)^{1/4} \times \left(\frac{\kappa_{\text{IR}}/\kappa_{\text{T}}}{20}\right)^{1/4} \left(\frac{\kappa_{\text{UV}}/\kappa_{\text{T}}}{2000}\right)^{1/4} \left(\frac{R_{\text{in}}}{r_{\text{ds}}}\right)^{-1/2} \text{ km s}^{-1} \quad (34)$$

and

$$\dot{M} \sim 0.1 \left(\frac{M}{10^7 M_{\odot}}\right)^{3/4} \left(\frac{L_{\text{UV}}/L_{\text{E}}}{0.1}\right)^{3/4} \times \left(\frac{\kappa_{\text{IR}}/\kappa_{\text{T}}}{20}\right)^{-1/4} \left(\frac{\kappa_{\text{UV}}/\kappa_{\text{T}}}{2000}\right)^{-1/4} \left(\frac{R_{\text{in}}}{r_{\text{ds}}}\right)^{1/2} M_{\odot} \text{ yr}^{-1}. \quad (35)$$

Outflows with speeds from ~ 100 to $\sim 2000 \text{ km s}^{-1}$ have been identified in observations of X-ray warm absorbers (e.g., Kaastra et al. 2000; Kaspi et al. 2000) and UV absorbers (e.g., Anderson & Kraft 1969; Crenshaw et al. 1999) in Seyfert 1s. Mass loss rates inferred from X-ray warm absorbers go from $\sim 10^{-3}$ to $\sim 10 M_{\odot} \text{ yr}^{-1}$ (e.g., Blustin et al. 2005; Zhang et al. 2011), whereas studies of UV absorbers suggest a wider range of $\sim 10^{-4}$ to $\sim 10 M_{\odot} \text{ yr}^{-1}$ (Crenshaw & Kraemer 2012). These empirical results are roughly consistent with our fiducial values of v_{∞} and \dot{M} .

The mass loss rate can be understood in a more intuitive fashion. The initial mass of the torus is $M_{\text{tor}} \equiv C_{\text{tor}} \times 2\pi\rho_{\text{in}}R_{\text{in}}^3$, where $C_{\text{tor}} \approx 4$ for our initial condition (§2.3.1). We define the lifetime of the torus against mass loss in the radiation-driven wind as $t_{\text{tor}} \equiv M_{\text{tor}}/\dot{M}$; from equation (26), we have

$$t_{\text{tor}}\Omega_{\text{in}} \sim \frac{1}{2} C_{\text{tor}} (\tau_{\text{T}}\tau_{\text{UV}})_{\text{in}}^{1/2} \left(\frac{L_{\text{UV}}}{L_{\text{E}}}\right)^{-1/2}. \quad (36)$$

In this equation, $\Omega_{\text{in}} = (GM/R_{\text{in}}^3)^{1/2}$ is the orbital frequency at the inner edge, and $(\tau_{\text{T,UV}})_{\text{in}} \equiv \rho_{\text{in}}R_{\text{in}}\kappa_{\text{T,UV}}$ stand for Thomson and UV optical depths evaluated with inner-edge values. Our simulations have $(\tau_{\text{T}})_{\text{in}} \sim 0.8$, $(\tau_{\text{UV}})_{\text{in}} \sim 64$, and $0.10 \leq L_{\text{UV}}/L_{\text{E}} \leq 0.15$, so $t_{\text{tor}}\Omega_{\text{in}} \sim 42$. Our torus remains inside the simulation domain for a shorter amount of time because the torus body moves radially outward at late times (§3.1). Our Thomson optical depth may be reasonable for real AGNs, but our UV optical depth is too small by a factor of $\gtrsim 10$, so we expect the lifetime of realistic tori against mass loss to be $\gtrsim 3$ times longer.

4.4. Balance between radiation-driven mass loss and mass resupply

A salient feature of simulations for all L_{UV} is a radiation-driven wind from the inner surface (§3.1). The wind always has temperatures below T_{ds} since it lies outside of the dust sublimation radius. Depending on the geometry of the inner edge, the wind can be found at higher latitudes than the torus body; this enhances the covering fraction, and hints at a connection between the wind and dust observed in the polar regions of NGC 424 (Hönig et al. 2012) and NGC 3783 (Hönig et al. 2013).

The radiation-driven wind is distinct from the thermally driven wind (Begelman et al. 1983) commonly discussed in the context of the torus (Krolik & Begelman 1986; Krolik & Kriss 2001; Blustin et al. 2005). The latter refers to gas lifted from the inner surface, exposed to ionizing radiation from the central source, and heated to the Compton temperature soon after its ionization parameter exceeds unity (Krolik et al. 1981). The mass loss rate due to the thermally driven wind is $\sim 0.4 M_{\odot} \text{ yr}^{-1}$ (Krolik & Begelman 1986), similar to that of the radiation-driven wind found in equation (35). The two winds could consequently augment each other despite their different physical properties.

The mass lost to these winds could be resupplied from the outside. A steady state could also obtain in which the IR optical depth across the body is approximately constant, so that the IR radiative flux does not become powerful enough to shove the body collectively outward (§3.1). A combined molecular and ionized gas inflow rate of $\sim 0.2 M_{\odot} \text{ yr}^{-1}$ has been observed down to $\sim 40 \text{ pc}$ in NGC 1097 (Fathi et al. 2013). Inflows of this magnitude at the outskirts of the torus suffice to replenish the mass loss given by equation (35).

Magnetic effects can strongly influence the resupply rate. Magnetohydrodynamic (MHD) turbulence stirred up by the magnetorotational instability could lead to outward angular momentum transport through the torus and subsequent accretion toward the inner edge. The ideal MHD condition holds even at extremely low ionization fractions (Blaes & Balbus 1994; Gammie 1996), which can be maintained by X-rays (Neufeld & Maloney 1995) if they carry a sizeable fraction of the energy in the UV (e.g., Zamorani et al. 1981). Indeed, magnetic fields have been detected on $\lesssim 30 \text{ pc}$ scales in the nucleus of NGC 1068 (Lopez-Rodriguez et al. 2015).

Recall that the steady-state mass inflow timescale in a disk is $\sim [\alpha(H/R)^2\Omega]^{-1}$, where H/R and Ω are the aspect ratio and orbital frequency of the disk. Accretion driven by MHD stresses has $0.01 \lesssim \alpha \lesssim 0.1$, so the inflow timescale is quite close to the torus lifetime calculated in equation (36) if, as here, $H/R \sim 1$. The relatively mild dependence of $t_{\text{tor}}\Omega_{\text{in}}$ on $L_{\text{UV}}/L_{\text{E}}$ suggests that equilibrium between inflow and outflow could be attained

over a wide range of luminosities.

The presence of MHD stresses can redistribute angular momentum in the torus, altering the distribution of IR radiation needed to achieve radial force balance against gravity; this change could in turn affect whether the torus is vertically supported. Magnetic fields could also remove angular momentum altogether from the torus through a magnetized wind (Blandford & Payne 1982; Königl & Kartje 1994).

4.5. Radial perturbation of the torus inner surface

The nonlinear development of the radial perturbation of the inner surface (§3.2) is reminiscent of the Rayleigh–Taylor instability (Rayleigh 1883; Taylor 1950). For $L_{UV}/L_E \geq 0.12$, the emergence of fingers and arcs from an originally smooth inner surface is a hallmark of the instability. For $L_{UV}/L_E = 0.11$, the azimuthal wavenumber of the most prominent mode of the perturbation decreases as the development of the perturbation becomes nonlinear; this mirrors the classical picture in which the fastest-growing mode of the perturbation of the interface separating the two fluids shifts from high wavenumbers in the linear regime to low wavenumbers in the nonlinear regime (e.g. Garabedian 1957; Chang 1959).

Since radiation and not a physical fluid is supporting the gas against gravity, it is more accurate to compare our simulations with the radiative Rayleigh–Taylor instability (Krolik 1977; Mathews & Blumenthal 1977; Jacquet & Krumholz 2011; Jiang et al. 2013). Figure 2 shows that in both linear and nonlinear regimes, wherever a part of the $\tau_{UV} = 1$ surface is farther from the origin, the region immediately radially outward of it has greater $R^2 \hat{\mathbf{e}}_R \cdot \mathbf{F}_{IR}$ because the optical depth to the outer surface is smaller; the perturbation grows as a consequence. This mechanism is similar to what Krolik (1977) described. Nonetheless, the cylindrical geometry of our simulations, as well as the presence of an acceleration gradient and differential rotation, complicates direct comparison with these previous analyses.

The amplification of the perturbation turns a smooth density distribution inhomogeneous; this kind of fragmentation process could provide a physical mechanism for the formation of dusty clumps often invoked to explain the observed broad ~ 1 to $\sim 100 \mu\text{m}$ bump in the SED of AGNs (Nenkova et al. 2002, 2008), the weak $9.7 \mu\text{m}$ silicate emission or absorption feature (Nenkova et al. 2002, 2008; Hönig et al. 2006), and the gentle radial temperature profile of dust within the central parsec of Circinus (Tristram et al. 2007).

Radiation-driven clump formation has already been reported in FLD simulations of super-Eddington outflows from axisymmetric accretion disks (Takeuchi et al. 2013) and from two-dimensional planar atmospheres (Takeuchi et al. 2014) where the dominant source of opacity is electron scattering. Clumps in these simulations are irregular and typically one optical depth across. Anisotropic structures are likewise observed in our three-dimensional simulations employing genuine RT, but they have multiple characteristic length scales. Magnetic fields certainly exist in the torus (Lopez-Rodriguez et al. 2015) and could change how fragments are formed and destroyed, but we must leave its study to future work.

5. CONCLUSIONS

We have conducted three-dimensional, time-dependent RHD simulations of AGN tori in which gas and radiation are evolved simultaneously, and IR and UV radiative fluxes are not approximated using arbitrary closure prescriptions. The simulations reveal that a smooth, geometrically and Compton thick torus is not very permeable to IR radiation, whereas the optically thin central hole allows IR radiation to escape immediately; therefore, the IR radiative flux is much stronger through the central hole than across the torus, and IR radiative support inside the torus is weaker than if the torus body were optically thin (§3.3). Meanwhile, IR radiation undergoing several reflections at the inner surface before leaving the central hole enhances the IR radiation energy density at the inner edge (§4.1) and reduces the luminosity needed to achieve marginal IR radiative support.

The inner surface experiences a spontaneous breaking of axisymmetry under radiation and differential rotation; the consequent radial perturbation amplifies rapidly with time (§3.2). The growth of the perturbation conjures up the picture of the radiative Rayleigh–Taylor instability, but with critical differences. The fragmentation of the inner surface alludes to a physical mechanism for the creation of clumps; however, the steady-state configuration of the fragments is not probed by our simulations and is likely affected by magnetic fields (§4.5).

Most importantly, a dusty wind can be launched from the inner surface by UV radiation and propelled outward by a combination of IR and UV radiation. The appearance of this wind is inevitable in a torus with vertical density stratification (§3.1). High dust opacity in the UV, along with the concentration of IR radiative flux into the vertical direction (§3.3), means the wind likely experiences an acceleration well above gravity. The radiation-driven wind carries momentum comparable to that in UV radiation (§3.4). It is also a powerful mechanism of mass loss with the capacity to remove an isolated torus within ~ 20 orbital periods at the inner edge (§4.3).

Our study calls attention for the first time to the possibility that UV radiation pressure acting on dust can drive a wind with speed and mass loss rate of the same order as values inferred from observations (§4.3), and with mass loss rate similar to the better-known thermally driven wind (§4.4). In order to achieve an approximate steady state against mass loss through both kinds of winds, any such torus must be furnished with a new inventory of mass every ~ 20 orbital periods. The strong variation of radiative support throughout the body (§3.1), the existence of a radiation-driven wind (§§3.1 and 3.4), and the growth of perturbations along the inner surface (§3.2), demonstrate that the internal structures of tori are unlikely ever to achieve strict hydrostatic equilibrium.

The authors thank Jim Stone, Yanfei Jiang, and Shane Davis for generously allowing Athena and its time-dependent RT module to be used for this project and for providing technical support. This research was partially supported by NASA/ATP grants NNX11AF49G and NNX14AB43G. The simulations were performed on the Johns Hopkins Homewood High-Performance Cluster.

APPENDIX

A. TIME-INDEPENDENT LONG-CHARACTERISTICS UV RT

We have developed a time-independent long-characteristics RT module to deal with UV radiation from a point source at the origin in cylindrical coordinates. Our ray-casting algorithm is similar to that of Amanatides & Woo (1987). We construct a ray from the source to the center of every cell in the simulation domain, extend it so that it reaches the far side of the destination cell, and then chop it up into segments, one for each cell the ray passes through. This ray-casting is done once, before the simulation starts. Our adoption of cylindrical coordinates means that we only need to solve the ray-casting problem in two dimensions. A subtlety of our algorithm is that, whenever a ray passes very close to a cell corner, we allow the ray to pass diagonally through it.

At the beginning of a time step, we compute the UV radiation energy density in the destination cell by

$$\frac{4\pi}{c} J_{UV} \equiv \frac{L_{UV}}{4\pi r^2 c} e^{-\tau_{UV}} \frac{\exp(\frac{1}{2}\tau_{UV}^*) - \exp(-\frac{1}{2}\tau_{UV}^*)}{\tau_{UV}^*}, \quad (\text{A1})$$

where L_{UV} is the luminosity of the source in the UV and \mathbf{r} is the displacement from the source to the destination cell. We determine the UV optical depth τ_{UV} by accumulating the products of the length of each segment and $\rho\kappa_{UV}$ averaged over the cell in which the segment lies; note that we consider only half of the length of the last segment in this exercise. The last factor in the equation comes from averaging J_{UV} over the entire last segment, which has UV optical depth τ_{UV}^* ; its inclusion improves the agreement of the UV energy and momentum absorption rate between runs at different resolutions, particularly at locations where $\tau_{UV} \lesssim 1$.

To arrive at the energy and momentum source terms of gas due to UV radiation, we remind ourselves of the RT equation in the form derived by Mihalas & Klein (1982):

$$\begin{aligned} \frac{1}{c} \frac{\partial I_{UV}}{\partial t} + \hat{\mathbf{n}} \cdot \nabla I_{UV} &= \left(-1 + \hat{\mathbf{n}} \cdot \frac{\mathbf{v}}{c}\right) \rho(\kappa_{UV} + \sigma_{UV}) I_{UV} \\ &+ \left(1 + 3 \hat{\mathbf{n}} \cdot \frac{\mathbf{v}}{c}\right) \rho(\kappa_{UV} B + \sigma_{UV} J_{UV}) - 2\rho\sigma_{UV} \frac{\mathbf{v}}{c} \cdot \mathbf{H}_{UV}. \end{aligned} \quad (\text{A2})$$

The zeroth and first angular moments of equation (A2) are

$$\begin{aligned} \frac{1}{c} \frac{\partial J_{UV}}{\partial t} + \nabla \cdot \mathbf{H}_{UV} &= \\ \rho\kappa_{UV}(B - J_{UV}) + \rho(\kappa_{UV} - \sigma_{UV}) \frac{\mathbf{v}}{c} \cdot \mathbf{H}_{UV} &\equiv -\frac{1}{4\pi} S_{UV}^e, \end{aligned} \quad (\text{A3})$$

$$\begin{aligned} \frac{1}{c} \frac{\partial \mathbf{H}_{UV}}{\partial t} + \nabla \cdot \mathbf{K}_{UV} &= \\ -\rho(\kappa_{UV} + \sigma_{UV}) \left(\mathbf{H}_{UV} - \frac{\mathbf{v}}{c} \cdot \mathbf{K}_{UV} \right) &+ \frac{\mathbf{v}}{c} \rho(\kappa_{UV} B + \sigma_{UV} J_{UV}) \equiv -\frac{c}{4\pi} \mathbf{S}_{UV}^m. \end{aligned} \quad (\text{A4})$$

Lowrie et al. (1999) pointed out that equations (A2) to (A4) do not give the correct equilibrium in moving fluids. To overcome this problem, the time-dependent RT module of Athena solves the modified equation (4), but equations (A2) and (4) are identical to first order in v/c save for the subscripts.

For time-independent RT, which applies to the UV, we drop the time derivatives from equations (A2) to (A4). In the special case of point-source UV radiation interacting with purely absorbing material that does not re-radiate in the UV, we set $\sigma_{UV} = 0$, $B = 0$, $\mathbf{H}_{UV} = \hat{\mathbf{e}}_r J_{UV}$, and $\mathbf{K}_{UV} = \hat{\mathbf{e}}_r \hat{\mathbf{e}}_r J_{UV}$ in equations (A3) and (A4); the source terms we seek can be skimmed off as

$$-\frac{1}{4\pi} S_{UV}^e \equiv -\rho\kappa_{UV} J_{UV} \left(1 - \hat{\mathbf{e}}_r \cdot \frac{\mathbf{v}}{c}\right), \quad (\text{A5})$$

$$-\frac{c}{4\pi} \mathbf{S}_{UV}^m \equiv -\rho\kappa_{UV} J_{UV} \hat{\mathbf{e}}_r \left(1 - \hat{\mathbf{e}}_r \cdot \frac{\mathbf{v}}{c}\right). \quad (\text{A6})$$

Observe that a consistent solution cannot be reached with equations (5) and (6).

As implied by equations (2) and (3), the source terms are added directly to the gas at the beginning of the time step. The energy source term is rather large compared to the other terms of equation (3), so the gas is temporarily overheated. The IR radiative sub-step is then carried out as described by Jiang et al. (2014), during which the gas releases almost all of the energy it gained from the UV into the IR. Although the source terms are added using the explicit Euler method, the IR radiative sub-step proceeds by the implicit Euler method, hence a large energy source term does not pose a problem.

Despite the sharp rise in gas temperature after the UV long-characteristics sub-step, we must not change the IR and UV opacities until the IR radiative sub-step is finished; otherwise, gas exposed to UV radiation would be absorbing UV and emitting IR at two unrelated opacities, which would generate specious temperature fluctuations with a period equal to two or three time steps around the true equilibrium value.

B. REDUCED SPEED OF LIGHT APPROXIMATION

The radiative timescale governing equations (4) to (6) is shorter than the hydrodynamic timescale of equations (1) to (3) by a factor of $c/v \gg 1$. Our primary concern is the hydrodynamic timescale, whereas the fast variation of I_{IR} relative to ρ , \mathbf{v} , and p is uninteresting since radiation merely equilibrates with the gas in between hydrodynamic time steps. To avoid following the system on the radiative timescale, we adopt the method of reduced speed of light (Gnedin & Abel 2001; Skinner & Ostriker 2013).

The physical light speed c attached to the time derivatives in equations (4) to (6) is substituted with the reduced light speed \hat{c} . This allows the use of coarser temporal resolution since the rate of change of I_{IR} in equation (4), including thermalization by absorption, isotropization by scattering, propagation in vacuum, and advection in optically thick gas, is slowed down by a factor of \hat{c}/c . The source terms S_{IR}^e and \mathbf{S}_{IR}^m are not altered, only the rate at which they change J_{IR} and \mathbf{H}_{IR} in equations (5) and (6); in fact, they must not be touched in equations (2) and (3) if we are to preserve gas dynamics.

Our approximation does not stop radiation from reaching equilibrium with the gas inasmuch as $v < \hat{c} \ll c$. However, it is critical that we not replace c attached to \mathbf{v}/c in equations (4) to (6), otherwise \mathbf{H}_{IR} could be beamed in the direction of \mathbf{v} even when $v \lesssim \hat{c} \ll c$.

Because the rate of change of energy and momentum of gas is c/\hat{c} times that of radiation, equations (2), (3), (5) and (6) taken together do not conserve the physical values of energy

and momentum, but $E + 4\pi J_{\text{IR}}/\hat{c}$ and $\rho \mathbf{v} + 4\pi \mathbf{H}_{\text{IR}}/(c\hat{c})$ instead. Granted that spurious transients may manifest themselves on approach to energy and momentum equilibrium between gas and radiation, we nevertheless expect time-averaged values of S_{IR}^e and \mathbf{S}_{IR}^m to vanish once equilibrium prevails.

A technical point to bear in mind is that the time-dependent RT module of Athena evaluates $S_{\text{IR}}^e \Delta t$ and $\mathbf{S}_{\text{IR}}^m \Delta t$ not from the right-hand sides of equations (5) and (6), but directly from ΔI_{IR} as computed by the IR radiative sub-step; the conversion from ΔI_{IR} to $S_{\text{IR}}^e \Delta t$ and $\mathbf{S}_{\text{IR}}^m \Delta t$ therefore necessitates a factor of c/\hat{c} .

C. IMPROVEMENT TO TREATMENT OF SCATTERING IN ATHENA

We consider the treatment of scattering opacity by the time-dependent RT module of Athena. The notation follows Jiang et al. (2014), except that here c and \hat{c} are the physical and reduced light speeds. We define σ_s as the scattering cross section per volume, Δt as the time step, and $\zeta \equiv \tau_s^* v/c$, where $\tau_s^* \equiv \sigma_s \hat{c} \Delta t$.

The module handles scattering by solving equations (29) and (30) listed in the reference. We repeat the equations below, minus a couple typos:

$$\begin{pmatrix} a_1+b_1+c_1 & b_2+c_1 & b_3+c_1 & \cdots & b_N+c_1 \\ b_1+c_2 & a_2+b_2+c_2 & b_3+c_2 & \cdots & b_N+c_2 \\ b_1+c_3 & b_2+c_3 & a_3+b_3+c_3 & \cdots & b_N+c_3 \\ \vdots & \vdots & \vdots & \ddots & \vdots \\ b_1+c_N & b_2+c_N & b_3+c_N & \cdots & a_N+b_N+c_N \end{pmatrix} \begin{pmatrix} x_1 \\ x_2 \\ x_3 \\ \vdots \\ x_N \end{pmatrix} = \begin{pmatrix} r_1 \\ r_2 \\ r_3 \\ \vdots \\ r_N \end{pmatrix}, \quad (\text{A7})$$

where

$$a_l \equiv W_l^{-1} [1 + \tau_s^* (1 - \mathbf{n}_l \cdot \mathbf{v}/c)], \quad (\text{A8a})$$

$$b_l \equiv \tau_s^* [2(\mathbf{n}_l \cdot \mathbf{v}/c) - (\mathbf{n}_l \cdot \mathbf{v}/c)^2 - v^2/c^2], \quad (\text{A8b})$$

$$c_l \equiv -\tau_s^* [1 + 3(\mathbf{n}_l \cdot \mathbf{v}/c)], \quad (\text{A8c})$$

$$x_l \equiv W_l I_l^{n+1}, \quad (\text{A8d})$$

$$r_l \equiv I_l^n. \quad (\text{A8e})$$

In the process of computing the LU decomposition of the matrix, $c_l - c_N \sim \zeta$ appears multiple times in the denominator. If $\zeta \ll 1$, some elements of the resultant matrices are ~ 1 while others are $\sim \zeta^{-1}$; put differently, the matrices are ill-conditioned, with the ratio of the greatest to smallest singular values of either matrix being $\sim \zeta$. Because the solution is computed using back-substitution as $x_i = U_{ij}^{-1} L_{jk}^{-1} r'_k$, it could be highly inaccurate. The code already includes checks to avoid this kind of situation, but it is easy to construct triples of τ_s^* , v , and c that bypass them.

When ζ is below a certain threshold, it is preferable to regard the scattering equation, written in the form

$$I_l^n = \sum_{m=1}^N (\lambda_{lm} + \epsilon_{lm}) I_m^{n+1}, \quad (\text{A9})$$

where

$$\lambda_{lm} \equiv (1 + \tau_s^*) \delta_{lm} - \tau_s^* W_m, \quad (\text{A10a})$$

$$\epsilon_{lm} \equiv \tau_s^* (a'_l \delta_{lm} + b'_m W_m + c'_l W_m), \quad (\text{A10b})$$

$$a'_l \equiv -\mathbf{n}_l \cdot \mathbf{v}/c, \quad (\text{A10c})$$

$$b'_l \equiv 2(\mathbf{n}_l \cdot \mathbf{v}/c) - (\mathbf{n}_l \cdot \mathbf{v}/c)^2, \quad (\text{A10d})$$

$$c'_l \equiv -[3(\mathbf{n}_l \cdot \mathbf{v}/c) + v^2/c^2], \quad (\text{A10e})$$

and δ_{lm} is the Kronecker delta, as a perturbative equation and solve it iteratively. The procedure starts with $I_l^{n+1} \leftarrow I_l^n$; each iterative step updates the solution as

$$I_l^{n+1} \leftarrow \sum_{m=1}^N \lambda_{lm}^{-1} \left[I_m^n - \sum_{p=1}^N \epsilon_{mp} I_p^{n+1} \right]. \quad (\text{A11})$$

The special structure of the matrix allows the inner multiplication to be accomplished with time expenditure $O(N)$, while the multiplication of any vector v_m by the inverse matrix λ_{lm}^{-1} is simply

$$\sum_{m=1}^N \lambda_{lm}^{-1} v_m = \frac{1}{1 + \tau_s^*} \left(v_l + \tau_s^* \sum_{m=1}^N W_m v_m \right) \quad (\text{A12})$$

since $\sum_{m=1}^N W_m = 1$. The chief aim of this modification is not to obtain a more accurate solution when $\zeta \sim 10^{-15}$; rather, it prevents the numerical instability that the standard algorithm exhibits in the static or extremely optically thin limit. Furthermore, the new solution is not to replace, but to complement, the old solution.

The threshold at which we switch between solution strategies is somewhat arbitrary; our choice is $\zeta = 10^{-5}$ as the standard algorithm has not yet shown instability above it. If double-precision floating-point numbers are used, the machine epsilon is $2^{-52} \approx 2.22 \times 10^{-16}$, so the iterative step should be performed at least four times.

D. IR INITIAL CONDITION

Because the time-dependent RT module of Athena operates on I_{IR} rather than J_{IR} and \mathbf{H}_{IR} , we must convert E_{IR}^0 provided by the initial condition to I_{IR} . Inside the optically thick torus body, the IR specific intensity in the fluid frame can be found in the FLD approximation as (Levermore & Pomraning 1981)

$$I_{\text{IR}}^0(\hat{\mathbf{n}}^0) \equiv \frac{c}{4\pi} E_{\text{IR}}^0 \mathcal{R}^{-1} (\coth \mathcal{R} - \hat{\mathbf{m}}^0 \cdot \hat{\mathbf{n}}^0)^{-1}; \quad (\text{A13})$$

it follows that

$$\mathbf{H}_{\text{IR}}^0 = \frac{c}{4\pi} E_{\text{IR}}^0 (\coth \mathcal{R} - \mathcal{R}^{-1}) \hat{\mathbf{m}}^0. \quad (\text{A14})$$

Here $\mathcal{R} \equiv \|\nabla E_{\text{IR}}^0\|/(\rho \kappa_{\text{IR}} E_{\text{IR}}^0)$ is the Knudsen number for radiation diffusion, and $\hat{\mathbf{m}}^0 \equiv -\nabla E_{\text{IR}}^0/\|\nabla E_{\text{IR}}^0\|$. Geometrically speaking, if we draw arrows $\hat{\mathbf{n}}^0$ from the origin with lengths proportional to $I_{\text{IR}}^0(\hat{\mathbf{n}}^0)$, the envelope is a prolate ellipsoid with ellipticity $\tanh \mathcal{R}$ and one focus at the origin. We impose the additional constraint that $0 \leq \tanh \mathcal{R} \leq 0.95$; the ceiling makes radiation less unidirectional in optically thin regions so that at least a few grid rays carry finite specific intensity. The specific intensity is then boosted to the observer frame by

$$I_{\text{IR}}(\hat{\mathbf{n}}) = I_{\text{IR}}^0(\hat{\mathbf{n}}^0) \left[\frac{(1 - v^2/c^2)^{1/2}}{1 - \hat{\mathbf{n}} \cdot \mathbf{v}/c} \right]^4. \quad (\text{A15})$$

We remarked after equation (4) that I_{IR} is a frequency-integrated quantity, which explains why the exponent is four, not three. Note that the FLD approximation is used merely to define the initial condition; it is not used to solve equations (4) to (6).

E. ORBITAL VELOCITY PROFILE OF A HYDROSTATIC, RADIATION-SUPPORTED TORUS

The force balance of a hydrostatic torus supported by IR radiation against the gravity of a point mass is expressed in

$$-\nabla\left(-\frac{GM}{r}\right) + \frac{\kappa_{\text{IR}}}{c}\mathbf{F}_{\text{IR}} + \frac{v_\phi^2}{R}\hat{\mathbf{e}}_R = \mathbf{0}. \quad (\text{A16})$$

The equation is solved together with the constraint of IR radiation energy conservation, $\nabla \cdot \mathbf{F}_{\text{IR}} = 0$, and the assumption that κ_{IR} is not a strong function of position. A similar equation has been solved by Krolik (2007) under axisymmetry; here we present a more intuitive approach. Because the gravitational and radiative terms are both divergence-free, the same must also be true for $(v_\phi^2/R)\hat{\mathbf{e}}_R$. The only radial and divergence-free vector field is $C(\phi, z)R^{-1}\hat{\mathbf{e}}_R$ for some function $C(\phi, z)$, hence v_ϕ is a constant over R . If we further restrict v_ϕ to be axisymmetric, we can write

$$v_\phi(R, z) = j_{\text{in}}(z)\left(\frac{GM}{R_{\text{in}}}\right)^{1/2}. \quad (\text{A17})$$

Here $j_{\text{in}}(z)$ is some dimensionless function that measures the shortfall of orbital velocity at $R = R_{\text{in}}$ from Keplerian as a consequence of radiative support, so we have $0 \leq j_{\text{in}} \leq 1$.

REFERENCES

- Amanatides, J., & Woo, A. 1987, in *Eurographics '87*, ed. G. Maréchal (New York: North-Holland), 3
- Anderson, K. S., & Kraft, R. P. 1969, *ApJ*, **158**, 859
- Antonucci, R. R. J., & Miller, J. S. 1985, *ApJ*, **297**, 621
- Antonucci, R. 1993, *ARA&A*, **31**, 473
- Barthel, P. D. 1989, *ApJ*, **336**, 606
- Barvainis, R. 1987, *ApJ*, **320**, 537
- Beckert, T., Driebe, T., Hönig, S. F., & Weigelt, G. 2008, *A&A*, **486**, L17
- Begelman, M. C., McKee, C. F., & Shields, G. A. 1983, *ApJ*, **271**, 70
- Blaes, O. M., & Balbus, S. A. 1994, *ApJ*, **421**, 163
- Blandford, R. D., & Payne, D. G. 1982, *MNRAS*, **199**, 883
- Blustin, A. J., Page, M. J., Fuerst, S. V., Branduardi-Raymont, G., & Ashton, C. E. 2005, *A&A*, **431**, 111
- Burtscher, L., Jaffe, W., Raban, D., et al. 2009, *ApJL*, **705**, L53
- Burtscher, L., Meisenheimer, K., Tristram, K. R. W., et al. 2013, *A&A*, **558**, 149
- Chang, C. T. 1959, *PhFl*, **2**, 656
- Cid Fernandes, R., Heckman, T., Schmitt, H., González Delgado, R. M., & Storchi-Bergmann, T. 2001, *ApJ*, **558**, 81
- Clavel, J., Wamsteker, W., & Glass, I. S. 1989, *ApJ*, **337**, 236
- Crenshaw, D. M., & Kraemer, S. B. 2012, *ApJ*, **753**, 75
- Crenshaw, D. M., Kraemer, S. B., Boggess, A., et al. 1999, *ApJ*, **516**, 750
- Davies, R. I., Burtscher, L., Rosario, D., et al. 2015, *ApJ*, **806**, 127
- Davies, R. I., Müller Sánchez, F., Genzel, R., et al. 2007, *ApJ*, **671**, 1388
- Davis, S. W., Stone, J. M., & Jiang, Y.-F. 2012, *ApJS*, **199**, 9
- Dorodnitsyn, A., Bisnovatyi-Kogan, G. S., & Kallman, T. 2011, *ApJ*, **741**, 29
- Dorodnitsyn, A., & Kallman, T. 2012, *ApJ*, **761**, 70
- Dorodnitsyn, A., Kallman, T., & Bisnovatyi-Kogan, G. S. 2012, *ApJ*, **747**, 8
- Dorodnitsyn, A., Kallman, T., & Proga, D. 2016, *ApJ*, **819**, 115
- Elitzur, M., & Shlosman, I. 2006, *ApJL*, **648**, L101
- Fathi, K., Lundgren, A. A., Kohno, K., et al. 2013, *ApJL*, **770**, L27
- Gammie, C. F. 1996, *ApJ*, **457**, 355
- Garabedian, P. R. 1957, *Royal Society of London Proceedings Series A*, **241**, 423
- Gnedin, N. Y., & Abel, T. 2001, *NewA*, **6**, 437
- Goldreich, P., Goodman, J., & Narayan, R. 1986, *MNRAS*, **221**, 339
- González Delgado, R. M., Heckman, T., & Leitherer, C. 2001, *ApJ*, **546**, 845
- Goodrich, R. W. 1989, *ApJ*, **340**, 190
- Heckman, T. M., González-Delgado, R., Leitherer, C., et al. 1997, *ApJ*, **482**, 114
- Hönig, S. F., Beckert, T., Ohnaka, K., & Weigelt, G. 2006, *A&A*, **452**, 459
- Hönig, S. F., Kishimoto, M., Antonucci, R., et al. 2012, *ApJ*, **755**, 149
- Hönig, S. F., Kishimoto, M., Tristram, K. R. W., et al. 2013, *ApJ*, **771**, 87
- Hopkins, P. F., Hayward, C. C., Narayanan, D., & Hernquist, L. 2012, *MNRAS*, **420**, 320
- Hopkins, P. F., Torrey, P., Faucher-Giguère, C.-A., Quataert, E., & Murray, N. 2016, *MNRAS*, **458**, 816
- Hueyotl-Zahuanitla, F., Palouš, J., Wunsch, R., Tenorio-Tagle, G., & Silich, S. 2013, *ApJ*, **766**, 92
- Jacquet, E., & Krumholz, M. R. 2011, *ApJ*, **730**, 116
- Jaffe, W., Meisenheimer, K., Röttgering, H. J. A., et al. 2004, *Natur*, **429**, 47
- Jiang, Y.-F., Davis, S. W., & Stone, J. M. 2013, *ApJ*, **763**, 102
- Jiang, Y.-F., Stone, J. M., & Davis, S. W. 2012, *ApJS*, **199**, 14
- . 2014, *ApJS*, **213**, 7
- Kaasra, J. S., Mewe, R., Liedahl, D. A., Komossa, S., & Brinkman, A. C. 2000, *A&A*, **354**, L83
- Kartje, J. F., Königl, A., & Elitzur, M. 1999, *ApJ*, **513**, 180
- Kaspi, S., Brandt, W. N., Netzer, H., et al. 2000, *ApJL*, **535**, L17
- Keating, S. K., Everett, J. E., Gallagher, S. C., & Deo, R. P. 2012, *ApJ*, **749**, 32
- Kishimoto, M., Hönig, S. F., Antonucci, R., et al. 2009, *A&A*, **507**, L57
- Kishimoto, M., Hönig, S. F., Antonucci, R., et al. 2011a, *A&A*, **527**, 121
- Kishimoto, M., Hönig, S. F., Antonucci, R., et al. 2011b, *A&A*, **536**, 78
- Kishimoto, M., Hönig, S. F., Antonucci, R., et al. 2013, *ApJL*, **775**, L36
- Königl, A., & Kartje, J. F. 1994, *ApJ*, **434**, 446
- Krolik, J. H. 1977, *PhFl*, **20**, 364
- Krolik, J. H., & Begelman, M. C. 1986, *ApJL*, **308**, L55
- Krolik, J. H., McKee, C. F., & Tarter, C. B. 1981, *ApJ*, **249**, 422
- Krolik, J. H. 2007, *ApJ*, **661**, 52
- Krolik, J. H., & Begelman, M. C. 1988, *ApJ*, **329**, 702
- Krolik, J. H., & Kriss, G. A. 2001, *ApJ*, **561**, 684
- Lawrence, A., & Elvis, M. 2010, *ApJ*, **714**, 561
- Levermore, C. D., & Pomraning, G. C. 1981, *ApJ*, **248**, 321
- López-Gonzaga, N., Burtscher, L., Tristram, K. R. W., Meisenheimer, K., & Schartmann, M. 2016, arXiv: 1602.05592
- Lopez-Rodriguez, E., Packham, C., Jones, T. J., et al. 2015, *MNRAS*, **452**, 1902
- Lovelace, R. V. E., Romanova, M. M., & Biermann, P. L. 1998, *A&A*, **338**, 856
- Lowrie, R. B., Morel, J. E., & Hittinger, J. A. 1999, *ApJ*, **521**, 432
- MacAlpine, G. M. 1985, in *Astrophysics of Active Galaxies and Quasi-Stellar Objects*, ed. J. S. Miller (Mill Valley, CA: University Science Books), 259

- Mathews, W. G., & Blumenthal, G. R. 1977, *ApJ*, **214**, 10
- Meisenheimer, K., Tristram, K. R. W., Jaffe, W., et al. 2007, *A&A*, **471**, 453
- Merloni, A., Bongiorno, A., Brusa, M., et al. 2014, *MNRAS*, **437**, 3550
- Mihalas, D., & Klein, R. I. 1982, *JCoPh*, **46**, 97
- Mihalas, D., & Weibel-Mihalas, B. 1984, *Foundations of Radiation Hydrodynamics* (New York: Oxford University Press)
- Miller, J. S., & Goodrich, R. W. 1990, *ApJ*, **355**, 456
- Nenkova, M., Ivezić, Ž., & Elitzur, M. 2002, *ApJL*, **570**, L9
- Nenkova, M., Sirocky, M. M., Nikutta, R., Ivezić, Ž., & Elitzur, M. 2008, *ApJ*, **685**, 160
- Neufeld, D. A., & Maloney, P. R. 1995, *ApJL*, **447**, L17
- Oh, K., Yi, S. K., Schawinski, K., et al. 2015, *ApJS*, **219**, 1
- Ohsuga, K., & Umemura, M. 1999, *ApJL*, **521**, L13
- . 2001, *A&A*, **371**, 890
- Phinney, E. S. 1989, in *NATO Advanced Science Institutes Series C: Mathematical and Physical Science, Theory of Accretion Disks*, ed. F. Meyer, **Vol. 290** (Dordrecht: Kluwer), 457
- Pier, E. A., & Krolik, J. H. 1992a, *ApJL*, **399**, L23
- . 1992b, *ApJ*, **401**, 99
- . 1993, *ApJ*, **418**, 673
- Pogge, R. W. 1989, *ApJ*, **345**, 730
- Pogge, R. W., & De Robertis, M. M. 1993, *ApJ*, **404**, 563
- Poncellet, A., Perrin, G., & Sol, H. 2006, *A&A*, **450**, 483
- Pott, J.-U., Malkan, M. A., Elitzur, M., et al. 2010, *ApJ*, **715**, 736
- Raban, D., Jaffe, W., Röttgering, H., Meisenheimer, K., & Tristram, K. R. W. 2009, *MNRAS*, **394**, 1325
- Rayleigh, L. 1883, *Proceedings of the London Mathematical Society*, **14**, 170
- Rees, M. J., Silk, J. I., Werner, M. W., & Wickramasinghe, N. C. 1969, *Natur*, **223**, 788
- Rieke, G. H., & Lebofsky, M. J. 1981, *ApJ*, **250**, 87
- Risaliti, G., Maiolino, R., & Salvati, M. 1999, *ApJ*, **522**, 157
- Roth, N., Kasen, D., Hopkins, P. F., & Quataert, E. 2012, *ApJ*, **759**, 36
- Sanders, D. B., Phinney, E. S., Neugebauer, G., Soifer, B. T., & Matthews, K. 1989, *ApJ*, **347**, 29
- Schartmann, M., Meisenheimer, K., Klahr, H., et al. 2009, *MNRAS*, **393**, 759
- Semenov, D., Henning, Th., Helling, Ch., Ilgner, M., & Sedlmayr, E. 2003, *A&A*, **410**, 611
- Shi, J., & Krolik, J. H. 2008, *ApJ*, **679**, 1018
- Skinner, M. A., & Ostriker, E. C. 2013, *ApJS*, **206**, 21
- Stone, J. M., Gardiner, T. A., Teuben, P., Hawley, J. F., & Simon, J. B. 2008, *ApJS*, **178**, 137
- Swain, M., Vasisht, G., Akeson, R., et al. 2003, *ApJL*, **596**, L163
- Takeuchi, S., Ohsuga, K., & Mineshige, S. 2013, *PASJ*, **65**, 88
- . 2014, *PASJ*, **66**, 48
- Taylor, G. 1950, *RSPSA*, **201**, 192
- Thompson, T. A., Quataert, E., & Murray, N. 2005, *ApJ*, **630**, 167
- Tristram, K. R. W., Burtscher, L., Jaffe, W., et al. 2014, *A&A*, **563**, 82
- Tristram, K. R. W., Meisenheimer, K., Jaffe, W., et al. 2007, *A&A*, **474**, 837
- Tristram, K. R. W., Raban, D., Meisenheimer, K., et al. 2009, *A&A*, **502**, 67
- Tristram, K. R. W., Schartmann, M., Burtscher, L., et al. 2012, *JPhCS*, **372**, 2035
- Ueda, Y., Akiyama, M., Ohta, K., & Miyaji, T. 2003, *ApJ*, **598**, 886
- Urry, C. M., & Padovani, P. 1995, *PASP*, **107**, 803
- Wada, K. 2012, *ApJ*, **758**, 66
- . 2015, *ApJ*, **812**, 82
- Wada, K., & Norman, C. A. 2002, *ApJL*, **566**, L21
- Wilson, A. S. 1996, *VA*, **40**, 63
- Wittkowski, M., Kervella, P., Arsenault, R., et al. 2004, *A&A*, **418**, L39
- Zakamska, N. L., Schmidt, G. D., Smith, P. S., et al. 2005, *AJ*, **129**, 1212
- Zakamska, N. L., Strauss, M. A., Krolik, J. H., et al. 2006, *AJ*, **132**, 1496
- Zamorani, G., Henry, J. P., Maccacaro, T., et al. 1981, *ApJ*, **245**, 357
- Zhang, S. N., Ji, L., Marshall, H. L., et al. 2011, *MNRAS*, **410**, 2274